UNIVERSIDADE TECNOLÓGICA FEDERAL DO PARANÁ
DIRETORIA DE PESQUISA E PÓS-GRADUAÇÃO
PROGRAMA DE PÓS-GRADUAÇÃO EM ENGENHARIA QUÍMICA

JESSICA DO ROCIO DE PAULA DE OLIVEIRA

USE OF TANGERINE PEEL EXTRACTS FOR THE SYNTHESIS OF MAGNETIC NANOCATALYSTS APPLIED TO THE DEGRADATION OF PARACETAMOL

MASTER THESIS

PONTA GROSSA
2021

JESSICA DO ROCIO DE PAULA DE OLIVEIRA

USE OF TANGERINE PEEL EXTRACTS FOR THE SYNTHESIS OF MAGNETIC NANOCATALYSTS APPLIED TO THE DEGRADATION OF PARACETAMOL

Uso de extrato de cascas de tangerina para a síntese de nanocatalisadores magnéticos aplicados à degradação do Paracetamol

Master's work presented as a requirement to obtain a Master's Degree in Chemical Engineering from the Programa de Pós-Graduação em Engenharia Química, Universidade Tecnológica Federal do Paraná.

Supervisor: Dra. Giane Gonçalves Lenzi
Co-supervisor: Dr. Helder Teixeira Gomes

PONTA GROSSA
2021

Ministério da Educação
Universidade Tecnológica Federal do Paraná
Câmpus Ponta Grossa

JESSICA DO ROCIO DE PAULA DE OLIVEIRA

USO DE EXTRATO DE CASCAS DE TANGERINA PARA A SÍNTESE DE NANOCATALISADORES MAGNÉTICOS APLICADO À DEGRADAÇÃO DO PARACETAMOL

Trabalho de pesquisa de mestrado apresentado como requisito para obtenção do título de Mestra Em Engenharia Química da Universidade Tecnológica Federal do Paraná (UTFPR). Área de concentração: Desenvolvimento De Processos.

Data de aprovação: 12 de Fevereiro de 2021.

Prof.a Giane Goncalves Lenzi, Doutorado - Universidade Tecnológica Federal do Paraná

Prof Eduardo Sidinei Chaves, Doutorado - Universidade Federal de Santa Catarina (Ufsc)

Prof.a Juliana Martins Teixeira De Abreu Pietrobelli, Doutorado - Universidade Tecnológica Federal do Paraná

Documento gerado pelo Sistema Acadêmico da UTFPR a partir dos dados da Ata de Defesa em 12/02/2021.

ACKNOWLEDGMENTS

Many people have facilitated the preparation of this work for both practical and scientific support as well as in an emotional and affective way. In this way, I extend my acknowledgement to all those who have been with me throughout this research. Professors, lab friends and everyone who provided research assistance, thank you very much!

Namely, I thank the supervising professors Dra. Giane Gonçalves Lenzi (I really want to be like you!) and Dr. Helder T. Gomes for the scientific support given by both and guidance in the project, as well as the encouragement of the academic career.

To the Graduate Program in Chemical Engineering at UTFPR-PG for all the assistance provided, as well as to CAPES (Coordenação de Aperfeiçoamento de Pessoal de Nível Superior) for financial support.

I also extend my thanks to all professors and collaborators who carried out the characterizations of the synthesized materials corroborating the result of this work.

I thank God for the gift of wisdom and for the inspiration of this research, faith makes us be strong not to give up in the face of obstacles.

Finally and not least, I thank my parents, sister, husband and daughters (who have worked with me in this research since my womb). Family support was essential, especially in the face of this pandemic moment, so that I could dedicate my time to the experiments and writing of the dissertation. Love you!

"Para tudo há um tempo, para cada coisa há um momento debaixo do céu. Assim, concluí que nada é melhor para o homem do que alegrar-se e procurar o bem-estar durante sua vida. Igualmente é dom de Deus que todos possam comer, beber e gozar do fruto de seu trabalho. E verifiquei que nada há de melhor para o homem do que alegrar-se com o fruto de seus trabalhos. Esta é a parte que lhe toca. Pois, quem lhe dará a conhecer o que acontecerá com o volver dos anos? ”

(Eclesiastes 3: 1,12-13,22)

ABSTRACT

This study describes the synthesis of an innovative nanomaterial (patent application number BR 1020210000317) composed of cobalt ferrite functionalized in niobium pentoxide $CoFe_2O_4@Nb_5O_2$ synthesized by green synthesis using tangerine peel extract. The material values the combination of a magnetic material (which allows easy recovery after application) with niobium pentoxide (whose metal is abundant in Brazilian territory). The synthesis was carried out with some temperature variations of the niobium calcination before joining with iron and cobalt salts and tangerine extract, the resulting materials were applied as catalysts in the degradation of Paracetamol by photocatalysis. The new materials were characterized by the following techniques: surface and pore analysis (S_{BET}, S_{EXT}, S_{mic}, V_{mic} and V_{TOTAL}), photoacoustic spectroscopy (PAS), point of zero charge (pH_{PZC}), scanning electron microscopy (SEM/EDS) and X-ray diffraction (XRD). The studied reaction parameters included pH, catalyst concentration and radiation variation (different powers for the mercury vapor lamp). The results indicated that the $CoFe_2O_4@Nb_5O_2$ nanocatalysts were efficient in the degradation of Paracetamol (up to 99% degradation), showing better results under conditions of pH 1.0, catalyst concentration 103 mg L^{-1}, under irradiation of the 250 W mercury vapor lamp (greater than 28 mW /cm²) at 240 minutes of the reaction.

Keywords: Green synthesis. Heterogeneous photocatalysis. Emerging pollutants.

RESUMO

Este estudo descreve a síntese de um nanomaterial inovador (pedido de patente número BR 1020210000317) composto por ferrita de cobalto funcionalizada em pentóxido de nióbio $CoFe_2O_4@Nb_5O_2$ sintetizado via síntese verde utilizando extrato de casca de tangerina. O material valoriza a junção de um material magnético (que possibilita a fácil recuperação após a aplicação) com o pentóxido de nióbio (cujo metal é abundante em território brasileiro). A síntese foi realizada com diferentes temperaturas de calcinação do nióbio antes da junção com sais de ferro e cobalto e extrato de tangerina, os materiais resultantes foram aplicados como catalisadores na degradação do Paracetamol por fotocatálise. Os novos materiais foram caracterizados através de análise superficial e de poros (S_{BET}, S_{EXT}, S_{mic}, V_{mic} e V_{TOTAL}), espectroscopia fotoacústica (PAS), ponto de carga zero (pH_{PZC}, microscopia eletrônica de varredura (MEV/EDS) e difração de raios-X (DRX). Os parâmetros de reação estudados incluíram pH, concentração de catalisador e variação de radiação (diferentes potências para a lâmpada de vapor de mercúrio). Os resultados indicaram que os nanocatalisadores $CoFe_2O_4@Nb_5O_2$ foram eficientes na degradação do Paracetamol (até 99% de degradação), apresentando melhores resultados em condições de pH 1,0, concentração de catalisador 103 mg L^{-1}, sob irradiação da lâmpada de vapor de mercúrio de 250 W (maior que 28 mW/cm²) aos 240 minutos da reação.

Palavras-chave: Síntese verde. Fotocatálise heterogênea. Poluentes emergentes.

LIST OF FIGURES

LIST OF TABLES

SUMMARY

1 INTRODUCTION

With the advancement of nanotechnology, many routes are used to create and optimize the synthesis of different nanomaterials, which gain special attention in several research due to the infinite possibilities of application. Among the most diverse means to synthesize and optimize nanomaterials there is a way that combines the use of plant extracts with solution combustion synthesis (SCS), which can be just called green synthesis.

Green synthesis is one of the new routes that generally stands out for the use of some biomaterial and/or environmentally friendly production. The use of plant extracts has been applied as a reducing agent for several synthesis pathways, mainly for obtaining magnetic nanomaterials. This type of synthesis, already tested for example with hibiscus flower extract and sesame seed extract, inspired the use of a source rich in citric acid, a reagent widely used in SCS.

Nanomaterials, when applied to catalysis, have some advantages, including a large surface-to-volume ratio compared to bulk materials, high catalytic activity, wide range of applications, among others. Magnetic nanocatalysts have been explored, proving, in addition to their efficiency, an easier separation (by magnetic means) at the end of the reaction. Some of the most common magnetic nanocatalysts are magnetite and cobalt ferrite.

Among the various processes of catalytic reactions appears photocatalysis, which uses a catalyst and a radiation source to catalyze the reaction. The most efficiently lately used photocatalysts are TiO_2 and Nb_2O_5 and their derivatives. Niobium is an abundant metal in Brazil, however still undervalued in its gross form. Niobium oxide as a carrier or support for certain transition metal oxides, promotes oxidation activity while maintaining stability.

The number of research on the catalysis of emerging pollutants (EPs) has increased. The EPs are pollutants that are found in small quantities in the environment and in wastewater, and that until recently were not considered harmful by the quantity found. However, it has been found that over the years they have been accumulating and it can now be a challenge to remove them during commonly used water treatment systems without using catalysts. Examples of EPs are pharmaceutical residues, endocrine disrupters, plasticizers, pesticides and personal hygiene products, among

others. Paracetamol is an EP found in sewage in the order of nano or micrograms per liter. However, the increase in consumption raises the concern of accumulation of this drug in the food chain.

In view of this general knowledge, it has been suggested the idea of creating a methodology that uses green synthesis to produce magnetic nanomaterials and that adds value to the product obtained, being degradation of paracetamol one of its applications.

Desiring the magnetic property conferred to nanocatalysts by the presence of cobalt ferrite and the performance of niobium pentoxide in photocatalysis, the objective of this work is to propose a method that uses tangerine peel extract to produce cobalt ferrite functionalized in niobium pentoxide. In addition, it is also objective to apply the nanocatalysts in the degradation of paracetamol via heterogeneous photocatalytic processes.

2 OBJECTIVES

2.1 GENERAL OBJECTIVE

Use extracts of tangerine peel (*Citrus reticulata)* to synthesize magnetic catalysts with cobalt (Co), iron (Fe) and niobium (Nb) for catalytic application to paracetamol (PCT) degradation.

2.2 SPECIFIC OBJECTIVES

- Produce extracts using tangerine peel (*Citrus reticulata)* and determine its reducing power;
- Synthesize complex magnetic nanoparticles of cobalt ferrite functionalized in niobium pentoxide ($CoFe_2O_4@Nb_2O_5$) using the tangerine peel extract as antioxidant agent;
- Characterize the synthesized nanoparticles by different techniques;
- Apply these nanoparticles as catalysts in the degradation of paracetamol;
- Evaluate the performance and efficiency of the nanocatalysts in the degradation of paracetamol by photocatalysis.
- Recover and reuse the catalysts for the best conditions found.

3 LITERATURE REVIEW

3.1 NANOCATALYSTS

Catalytic processes are essential for many industries. Optimization in catalysis can minimize the use of energy and raw materials, reducing waste to the environment (RUTGER A. VAN SANTEN, 1991). Catalysis can also be applied to the degradation of harmful components into more environmentally friendly components. Catalytic processes can be heterogeneous or homogeneous. In the homogeneous catalytic processes, the catalyst is in the same phase as the reactants and products (all compounds are in solution). On the other hand, in heterogeneous catalytic processes the catalyst exists in a different phase than the reactants (the catalyst is usually a solid and the reactants are gases or liquids). In this case, the reagents pass through a solid catalyst. Most chemical processes use heterogeneous catalysis (BHADURI; MUKESH, 2000; ERTL *et al*., 2008; ROSS, 2011). In either processes, catalysts are used to change (increasing or decreasing) the rate of reactions.

Brazilian research on catalysts started around 1970 (DUPONT, 2002). The advent of nanosciences has promoted the molecular approach, which is currently very useful for the production of selective and efficient heterogeneous catalysts that can be removed after the reaction and reused. Nanocrystals of just a few nanometers have high catalytic efficiency, related to their high contact area (AMETA; AMETA, 2007)

Nanocatalysts are nanomaterials (NMs) with a catalyst function that have dimensions in the order of nanometer (10^{-9} m). Magnetic nanocatalysts (MNC) are studied due to advantages such as easy recovery at the end of the process and the efficiency of the catalytic activity of the metals that compose them (RIBEIRO *et al*., 2017). Due to their potential applications, several methods of synthesis of magnetic nanoparticles (MNPs) have been studied in recent years. The choice of the method depends on the different phases and the compounds desired as a result.

3.2 METHODS OF SYNTHESIS OF THE MAGNETIC NANOPARTICLES

The main methods used to synthesized nanoparticles are: microemulsion, thermal decomposition, solvothermal, sonochemical, microwave, chemical vapor deposition, carbon arc, synthesis of laser pyrolysis, co-precipitation, solution

combustion synthesis (SCS) and reduction using plant extracts (RPE) (FARAJI; YAMINI; REZAEE, 2010; JESSICA R P OLIVEIRA, 2017).

In this work two synthesis methods were conciliated to produce nanocatalysts, solution combustion synthesis (SCS) and reduction using plant extracts (RPE). The method used can be characterized as Green Synthesis, because it fits the 12 principles of green chemistry, specifically the principles 1, 3, 5 and 7, which concern: 1.Prevent waste; 3.Design less hazardous chemical syntheses; 5.Use safer solvents and reaction conditions; 7.Use renewable feedstocks (UNITED STATES ENVIRONMENTAL PROTECTION AGENCY, ; ANASTAS; WARNER, 1998; KHARISSOVA *et al*., 2019)

SCS, also called sol-gel combustion, is a redox reaction that occurs in a homogenous aqueous solution between an oxidizer (e.g. metal nitrates) and a fuel (e.g. glycine, urea, citric acid, etc.). The main advantages are resultant nanoparticles with high specific surface area and high reactive activity, inexpensive starting materials, high yield, simple processing and apparatuses that render SCS as cost-effective and suitable for mass production (HUANG *et al*., 2016). It is a suitable method for the production of oxide nanomaterials, which prompted research on optimizations for the production of iron oxides via SCS (IANOȘ, 2014; SHANMUGAVEL *et al*., 2015; HUANG *et al*., 2016; VENTURINI *et al*., 2018; BHAGWAT *et al*., 2019; CHAVARRIAGA *et al*., 2020).

Also called green synthesis or biosynthesis, RPE is a simple and efficient method of method of synthesizing nanoparticles, commonly applied to the synthesis of (Fe_3O_4). Different plant species already used to obtain extracts (from leaves, flowers or seeds) for the synthesis of magnetic nanoparticles are indicated in

Table 1. In this method, the size and shape of the nanoparticles obtained will depend on the characteristic of the extract, the location of the plant from which it was extracted (i.e. leaves, fruits or seeds), the reaction temperature, stirring rate, pH and biological composition of the plant (such as flavonoids, terpenoids, amino acids, proteins or sugars), among other factors (MAKAROV *et al*., 2014).

Table 1 - Plants species already used to synthesize magnetic nanoparticles.

PLANT SPECIES	NANOMATERIAL	SIZE	REFERENCE
Hordeum vulgare **Rumex acetosa**	iron oxide	30 nm 10 - 40 nm	(MAKAROV *et al*., 2014)
Euphorbia milli **Datura innoxia** **Calotropis procera** **Tinospora cordifolia** **Tridax procumbens** **Cymbopogon citratus (lemon grass tea)**	iron nanoparticles	13 - 51 nm 58 - 106 nm 58 - 342 nm 13 - 95 nm 15 - 155 nm 43 - 342 nm	(SNEHA SHAH, SUMITA DASGUPTA, MOUSUMI CHAKRABORTY, RAJI VADAKKEKARA, 2014)
Green tea extract	iron nanoparticles	20 - 80 nm 40 - 60 nm	(WANG *et al*., 2014; WU *et al*., 2015)
Salvia officinalis	iron-polyphenol complex nanoparticles	5 - 25 nm	(WANG; FANG; MALLAVARAPU, 2015)
Amaranthus dubius	iron nanoparticles	43 - 220 nm	(HARSHINY; ISWARYA; MATHESWARAN, 2015)
Castanea sativa **Eucalyptus globulus** **Ulex europaeus** **Pinus pinaster**	iron oxide	uninformed	(MARTÍNEZ-CABANAS *et al*., 2016)
Citrullus lanatus	magnetite	20 nm	(PRASAD; GANGADHARA; VENKATESWARLU, 2016)

Source: own authorship.

Gingasu *et. al.* (2016) produced cobalt ferrite ($CoFe_2O_4$) using hibiscus flower extract (*Hibiscus rosa-sinensis*) (GINGASU *et al*., 2016a) and sesame seed extract (*Sesamum indicum L*) (GINGASU *et al*., 2016b). In both works, the synthesis occurred using modified solution combustion synthesis, adding the extracts mentioned on cobalt and iron nitrates. To obtain $CoFe_2O_4$ nanoparticles, the extracts can act as capping agents, reducing agents, stabilizing and/or chelating agents for “capturing” the metal ions; they can also play a fuel role. This type of green synthesis is proposed in this work.

3.3 TANGERINE EXTRACT

The citrus fruit production in Brazil is relevant in the world scenario, being orange the citrus fruit most produced by the country, however other citrus fruits such as tangerine also present significant production and trade. According with data issued by

the United States Department of Agriculture (USDA, 2020), the world production of tangerine was around 31 652 000 tons (recorded in January 2019/20). In 2019, the Brazilian production represented 984 897 tons, 3% of the world production, being 298 647 produced in the south of the country, equivalent to 30% of the Brazilian production (IBGE - PRODUÇÃO AGRÍCOLA MUNICIPAL, 2020).

Tangerine (mandarin), whose specific classification is *Citrus reticulata* (*C. reticulata*), is one of the most important citrus genera (DURMUŞ; ÇOLAK; KARAKÖSE, 2019). It is a fruit widely consumed, with high content of vitamin C, B complex, flavonoids, carotenoids and ascorbic acid, among others. Because of its large production, large quantities of tangerine waste go to landfills, aggravating the environmental problems of solid waste generation (RUEDA *et al*., 2020).

There are already some reported works on the synthesis of NMs from tangerine peels, as those represented in Table 2 with their nanomaterials and corresponding sizes.

The possibility of synthesizing nanocatalysts using *C. reticulata* extract is promising to know that it comes from a citrus fruit containing citric acid, and that this in turn can be used in SCS (mentioned in item 3.2). Given these circumstances, one of the objectives of this work is to create a methodology to apply the *C. reticulata* extract in the green synthesis of NMs via SCS.

Table 2 - Summary of nanomaterials synthesized from tangerine peels.

NANOMATERIAL	SIZE	PART OF THE TANGERINE	SYNTHESIS METHOD	REFERENCE
Manganese oxides supported in tangerine peel-derived carbon (MnOx/TPC)	9.4 - 38.2 nm	Tangerine peel-derived carbon	pyrolysis	(LI *et al*., 2018)
Zinc oxide (ZnO-NPs)	44 - 81 nm	Tangerine peel extract	spray pyrolysis system	(DURMUŞ; ÇOLAK; KARAKÖSE, 2019)
Titanium Dioxide Nanocrystals (TiO_2-NCs)	50 - 150 nm	Tangerine peel extract	green synthesis method	(RUEDA *et al*., 2020)
Silver nanoparticles (TPE-AgNPs)	around 45 nm	Tangerine peel extract	bio-reduction	(ITUEN *et al*., 2020)

Source: own authorship

3.4 COBALT FERRITE FUNCTIONALIZED WITH NIOBIUM PENTOXIDE

Cobalt ferrite ($CoFe_2O_4$) is among the most relevant ferrites due to the peculiarities of its properties such as great physical and chemical stability (GINGASU *et al*., 2016a; CARVALHO *et al*., 2018; RANI *et al*., 2018). This material can be applied to magneto-sensitive systems (LONG *et al*., 2015; RANI *et al*., 2018), to remove pollutants from water (AMIRI *et al*., 2017b; RIBEIRO *et al*., 2017; SONU *et al*., 2019), in drug delivery (AMIRI *et al*., 2017a; SHI *et al*., 2020) and in acid mine drainage treatments (KEFENI; MAMBA; MSAGATI, 2017).

Niobium is an abundant transition metal in Brazil, which has about 98% of the world's known niobium reserves, located mainly in the states of Amazonas, Goiás and Minas Gerais. The discovery of this metal in the Brazilian territory took place in the mid-1960s when the possible applications for this metal were not yet known. Currently, it is known that it is used in metallic alloys (such as steel), making them stronger and more malleable. It is also used in high technology (rocket engines), in the production of superconducting wires and in other industrial applications that make niobium to have high technological value (PESSOA, 2018)

The calcination temperature of niobium pentoxide influences its structure. If calcination is carried out up to 400 °C, Nb_2O_5 will have an amorphous structure. For temperatures above 400 °C, there are many contradictions in relation to its polymorphism, since not all crystalline phases are well known and studied, but they can present a pseudohexagonal structure, leaving some amorphous phase. At high temperatures, for example around 600 °C, it may have an orthorhombic structure, around 800 °C it may have a tetragonal structure and around 1000 °C a monoclinic structure (FALK *et al*., 2017; FIDELIS, 2019). The structure of niobium is relevant to the chosen catalysis method, because depending on the method, the structure will have a greater influence than the contact area (FALK *et al*., 2017), or it can be the opposite, or both having great influence.

Niobium and its properties have been studied as photocatalysts in the oxide form (Nb_2O_5) and/or combined with other compounds. Some studies report the efficiency of the photocatalytic activity of niobium oxide in the degradation of dyes in textile industries (SILVA *et al*., 2002), in the degradation of the herbicide Methylviologen (CASTRO *et al*., 2016) and in the abatement of air pollution (XIANG *et*

al., 2017). Concerning to formation of complex compounds, combinations with niobium already reported in the literature are presented in

Table 3.

In this perspective, the feasibility of synthesizing efficient nanophotocatalysts using magnetic materials, such as cobalt ferrites, together with niobium oxide (abundant in the Brazilian territory), looks promising for application in the degradation of pollutant found in water.

Table 3 - Compounds combined with niobium.

Niobium with…	REFERENCE
Aluminum, gallium and indium oxides	(PETRE *et al*., 2003)
Copper, nickel and cobalt based-catalysts	(GUARINO *et al*., 2014)
Barium ferrite	(XU *et al*., 2014)
Ruthenium	(AMJAD *et al*., 2015)
Iron oxide	(ALI; MOHD ZABIDI; SUBBARAO, 2012; GUARINO *et al*., 2014; GHOSH; SWAIN; VERMA, 2017)
Cobalt ferrite	(RAMCHANDRA KIRAN *et al*., 2014; CARVALHO *et al*., 2018)

Source: own authorship

3.5 ADVANCED OXIDATION PROCESSES

Wastewater has become increasingly complex, containing toxic and non-biodegradable organic compounds that are difficult to remove by conventional treatment methods. The so-called advanced oxidation processes (AOPs) have been efficient and widely used tools, as they can effectively oxidize and mineralize various persistent organic compounds. In this process, highly oxidizing hydroxyl radicals ($^{\bullet}OH$) are produced (standard reduction potential between +2.8 V and +2.0 V at pH 0 and 14, respectively), capable of degrading organic pollutants generating CO_2, H_2O and inorganic ions. Photocatalysis and wet peroxide catalytic oxidation (CWPO) are among the various types of catalytic reactions that are characterized as AOPs (ERTL *et al*., 2008; GOMES *et al*., 2011; RIBEIRO *et al*., 2017; SILVA, 2019).

3.5.1 Photocatalysis

Photocatalysis is a reaction carried out in the presence of light and of a semiconductor catalyst (photocatalyst). Photocatalytic reactions can be homogeneous or heterogeneous (AMETA; AMETA, 2007). Photocatalysis using semiconductors has been shown to be highly effective in the degradation of pollutants that are difficult to remove by other methodologies. The semiconductors mostly used as catalysts in this process are binary semiconductors like TiO_2, ZnO, Fe_2O_3, CdS and ZnS due to a favorable combination of their electronic structure, light absorbing properties, load transport characteristics and excited-state lifetime (AMETA; AMETA, 2007; ZHU; ZHOU, 2019).

Ameta and Ameta (2007), according to the fragment given in Figure 1, explain photocatalytic reactions.

> Photocatalytic reactions are initiated by the absorption of a photon with appropriate energy (hv) that is equal to or higher than the band gap energy (E_g) of the photocatalyst. The absorbed photon creates a charge separation as the electron (e^-) is elevated from the valence band (VB) of a semiconductor to the conduction band (CB), creating a hole (h^+) in the VB. This excited electron can reduce any substrate or react with electron acceptors such as O_2 present on the semiconductor surface or dissolved in water, reducing it to superoxide radical anion $\bullet O_2^-$. On the other hand, the hole can oxidize the organic molecule to form R^+, or react with −OH or H_2O, oxidizing them to •OH radicals. Other highly oxidant species such as peroxide radicals are also responsible for the heterogeneous photodecomposition of organic substrates. (AMETA; AMETA, 2007, p.2).

Figure 1 - Illustration to exemplify the photocatalysis.

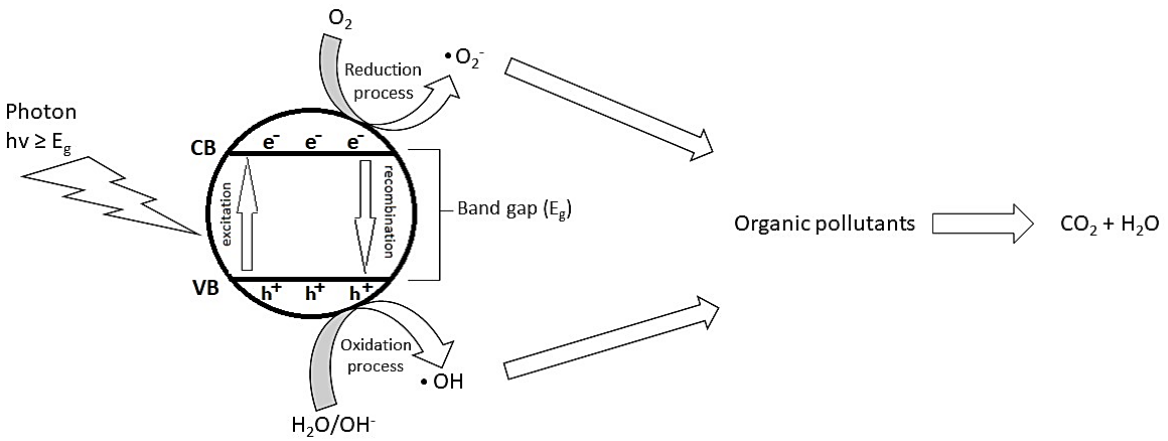

Source: own authorship

The previous definition of catalytic reaction is best understood with the definition of the following concepts, (KÖNIG, 2013):

- Photon: can be understood as an energy package;
- Bands and band gap: are terms related to the electronic structure of a solid. these terms describing, respectively, allowed and forbidden energetic states of electrons;
- Valence band (VB): referred the energetically highest bands populated by electrons in the ground state;
- Conduction band (CB): referred the lowest unpopulated bands.

Herrmann (1999) simplifies the explanation of a decomposition process by heterogeneous catalysis in five steps, later quoted by Rueda-Marquez et.al. (2020):

1. Transfer of pollutants to the photocatalyst's surface;
2. Adsorption of pollutants on the surface;
3. Photonic activation and decomposition of adsorbed molecules;
4. Desorption of reaction products;
5. Removal of reaction products from the photocatalyst's surface. (HERRMANN, 1999; RUEDA-MARQUEZ *et al*., 2020)

Photocatalysis has among its advantages the possibility of being used to degrade and mineralize dyes and chemicals into CO_2 and H_2O, being used in the degradation of very stable compounds that cannot be easily degraded by other processes, being an efficient process under ambient temperature and pressure conditions and by having low cost in relation to other oxidation processes (ZHANG *et al*., 2018).

Photocatalysis is used to degrade various harmful compounds in water treatment (FONTANA *et al*., 2018a; YU *et al*., 2020), mainly organic compounds (SONU *et al*., 2019; ZHU; ZHOU, 2019).

3.6 EMERGING POLLUTANTS

Studies and research on the quantity and types of waste generated by the population in recent times have increased, the proof of this is the emergence of

concepts such as emerging pollutants (EPs) and contaminants of emerging concern (CECs).

EPs are micropollutants considered persistent and refractory, which are currently not included in routine monitoring programs and which may be candidates for future regulation (NAPOLEÃO *et al*., 2015; MITRA *et al*., 2021; YADAV *et al*., 2021). EPs have been the subject of studies around the world, present in different environmental matrices in low concentration (μg L^{-1}, ng L^{-1}) and because they can represent a significant risk to human, ecological and environmental health, which are sometimes underestimated, makes them require alternative treatments capable of promoting their degradation. Examples of EP include surfactants, drugs, personal hygiene products, gasoline and plasticizers (NAPOLEÃO *et al*., 2015; VARGAS-BERRONES *et al*., 2020; MITRA *et al*., 2021).

It is suspected that CECs are present in several environmental compartments or introduced only recently in the environment and its effects on the environment and humans is still vastly unknown, but its toxicity or persistence is likely to alter the metabolism of a living being significantly. CECs can be naturally occurring, manufactured or manmade chemicals, for example, pharmaceuticals and personal care products, industrial and household chemicals, pesticides, manufactured nanomaterials, and their transformation products (MOLINARI *et al*., 2017; PESQUEIRA; PEREIRA; SILVA, 2020; VALBONESI *et al*., 2021; YADAV *et al*., 2021).

The concepts of EPs and CECs intersect with respect to pollutants that are being identified in low concentration in wastewater, which may require specific treatment for their removal, with only conventional treatments being inefficient. Advanced oxidative processes (AOPs) are among those alternatives. Drugs deserve special attention, as this type of substances are widely consumed by humans and administered to animals, resulting in discharges, usually of unknown concentrations, to the environment, especially in developing countries. (NAPOLEÃO *et al*., 2015; PAUMO *et al*., 2021)

3.6.1 Paracetamol

Paracetamol (or acetaminophen), the structure of which is depicted in Figure 2, is widely used worldwide as a drug without prescription. It is an analgesic and

antipyretic indicated for the relief of pain of mild to moderate intensity (AL-KAF *et al*., 2017; “Bula do Paracetamol”, 2020).

Figure 2 - Molecular structure of paracetamol.

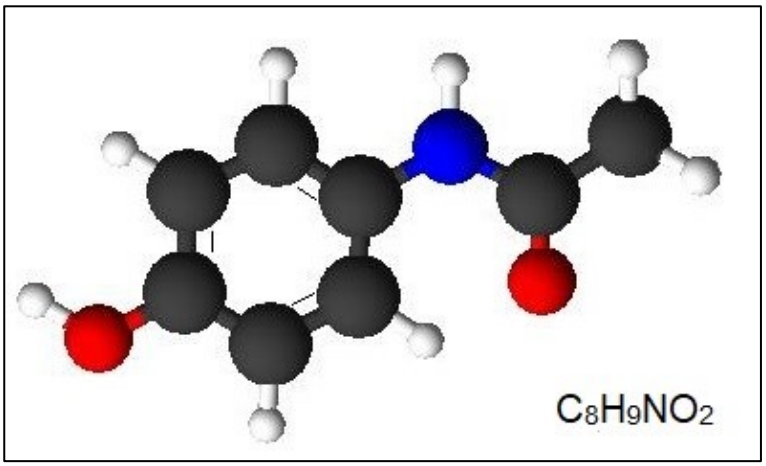

Source: own authorship

The main concern about increasing the consumption of this drug is that after ingested about 90% of a therapeutic dose is excreted in the urine after 24 hours. The composition of this excretion contains around 1-4% of unchanged paracetamol and 60-90% of metabolites (i.e., any intermediate compound in the metabolism's enzymatic reactions). It is found in sewage in the order of nano or micrograms per liter, being classified as an emerging pollutant. However, the increase in consumption raises the concern of accumulation of this drug in the food chain, since it is not easily degraded by the usual treatment methods at Wastewater Treatment Plants (WWTPs) (NAPOLEÃO *et al*., 2015; “FARMACOCINÉTICA PARACETAMOL”, 2016).

Several research studies have reported efficient degradation of paracetamol:

- by the action of microorganisms (WU; ZHANG; CHEN, 2012; AL-KAF *et al*., 2017; ŻUR *et al*., 2018).
- using catalytic processes, such as Fenton (CARRASCO-DÍAZ *et al*., 2017; AUGUSTO *et al*., 2018; SLAMANI *et al*., 2018);
- by Photo-Fenton (NAPOLEÃO *et al*., 2015; RAD *et al*., 2015; HINOJOSA GUERRA *et al*., 2019; BAVASSO; POGGI; PETRUCCI, 2020);
- by CWPO - catalytic wet peroxide oxidation (SANTOS SILVA *et al*., 2019);

- by photocatalysis (YANG; YU; RAY, 2008; MOCTEZUMA *et al*., 2012; JAGANNATHAN; GRIESER; ASHOKKUMAR, 2013; CALAS-BLANCHARD *et al*., 2015; ABDEL-WAHAB *et al*., 2017; JALLOULI *et al*., 2017; VAIANO; SACCO; MATARANGOLO, 2018; KHASAWNEH; PALANIANDY; TENG, 2019; WANG; BIAN, 2020).

Depending on the conditions and the reaction time, the works cited even managed to completely remove Paracetamol from the studied synthetic solution. It is expected that the innovative catalysts synthesized, when applied in a photocatalysis reaction, will achieve results as efficient as these.

4 METHODOLOGY

4.1 TANGERINE PEELS EXTRACT

The first step to obtain the catalyst is drying the tangerine peels, Figure 4 - Step 1 (A). The tangerine peels were collected of ripe and/or fallen fruit on a tree of a private property, located in the district of Uvaia, Ponta Grossa / PR (tree registered in the

Figure 3). Regarding these residues, that at most would become organic fertilizer or feed for the pigs, it was thought to make better use of the properties contained in the peels to apply them in the production of catalysts.

These peels further subjected to washing under continuous flow of water and previously drying under sun to avoid fungal contamination. After, the tangerine peels are placed in drying oven (SL 102, SOLAB) at 80 ± 5 °C for 18 h. Sequentially, the tangerine peels were crushed in an analytical mill (Q298A21, QUIMIS) and sieved to obtain a diameter between 250 μm (60 mesh) and 106 μm (150 mesh) (wire cloth test sieve, Bertel), Step 1 (B). Finally, the tangerine peels were stored until the next step.

To obtain the tangerine peels extract the following methodology was optimized, Step 1 (C), using an analytical balance (AUY220, SHIMADZU), 4.0 g of crushed tangerine peels were placed in a 250 mL round-bottom flask with 100 mL of distilled water, which was placed under magnetic stirring at room temperature (25 °C) for 3 h (C-MAG HS 7, IKA). After, the temperature was increased to 60 °C for 1 h (GINGASU *et al*., 2016a; NAVA *et al*., 2017), the dispersion further centrifuged at 4000 rpm (revolutions per minute) for 5 minutes, to separate the tangerine peels from the supernatant (80- 2B centrifuge, CENTRIBIO). After centrifugation, the supernatant was filtered through a paper filter, to remove any possible peel that was still present in the solution. Finally, the obtained extract solution was stored in a freezer until use, completing the first step, Step 1 (D). The reducing power (EC_{50} RP) of this extract was 1.68 ± 0.03 mg mL^{-1} (Analyzed by Centro de Investigação de Montanha - CIMO, Instituto Politécnico de Bragança, Bragança, Portugal). The EC_{50} values correspond to the concentration of extract that provides 50% of reducing power or antioxidant activity. Lower EC_{50} values means higher antioxidant capacity of the samples (OLIVEIRA *et al*., 2018).

Figure 3 - Tangerine tree, from which tangerines were collected for research.

Source: own authorship

4.2 REAGENTS

- Acetonitrile (CH_3CN), supplied by Merk, Germany.
- Anhydrous citric acid ($C_6H_8O_7$), supplied by Perquim Rep. Com., Analytical Science, Ponta Grossa- PR.
- Anhydrous sodium sulfate (Na_2SO_4), supplied by Neon, Suzano-SP.
- Cobalt nitrate ($Co(NO_3)_2.6H_2O$), supplied by Synth, Diadema-SP.
- Formic acid (CH_2O_2), supplied by Synth, Diadema-SP.
- Iron nitrate ($Fe(NO_3)_3.9H_2O$), supplied by Synth, Diadema-SP.
- Niobium pentoxide (Nb_2O_5), supplied by CBMM - Companhia Brasileira de Metalurgia e Mineração, Araxá-MG.
- Sodium hydroxide (NaOH), supplied by Dinâmica Química Contemporânea Ltda., Indaiatuba - SP.
- Sulfuric acid (H_2SO_4), supplied by Dinâmica Química Contemporânea Ltda., Indaiatuba - SP.

4.3 SYNTHESIS OF CATALYSTS

In preparation for the synthesis of the catalysts, the second step is niobium pentoxide calcination, Step 2 (E). Approximately 10 g of niobium pentoxide (Nb_2O_5, provided by CBMM-Companhia Brasileira de Metalurgia e Mineração, Araxá, Minas Gerais, Brazil) was weighted in a porcelain crucible. Then, each sample was calcined in a calcination furnace as shown in Table 4. This process resulted in seven samples of niobium oxide: Nb, Nb100, Nb200, Nb300, Nb400, Nb500 and Nb600.

Table 4 - Identification of niobium calcined samples

Sample name	**100 °C**	**200 °C**	**300 °C**	**400 °C**	**500 °C**	**600 °C**
Nb	Not calcined					
Nb100	for 1 h	-	-	-	-	-
Nb200	for 1 h	for 1 h	-	-	-	-
Nb300	for 1 h	for 1 h	for 1 h	-	-	-
Nb400	for 1 h	for 1 h	for 1 h	for 1 h	-	-
Nb500	for 1 h	for 1 h	for 1 h	for 1 h	for 1 h	-
Nb600	for 1 h	for 1 h	for 1 h	for 1 h	for 1 h	for 1 h

Source: own authorship

Figure 4 - Route to the green synthesis method of functionalized cobalt ferrite in niobium pentoxide.

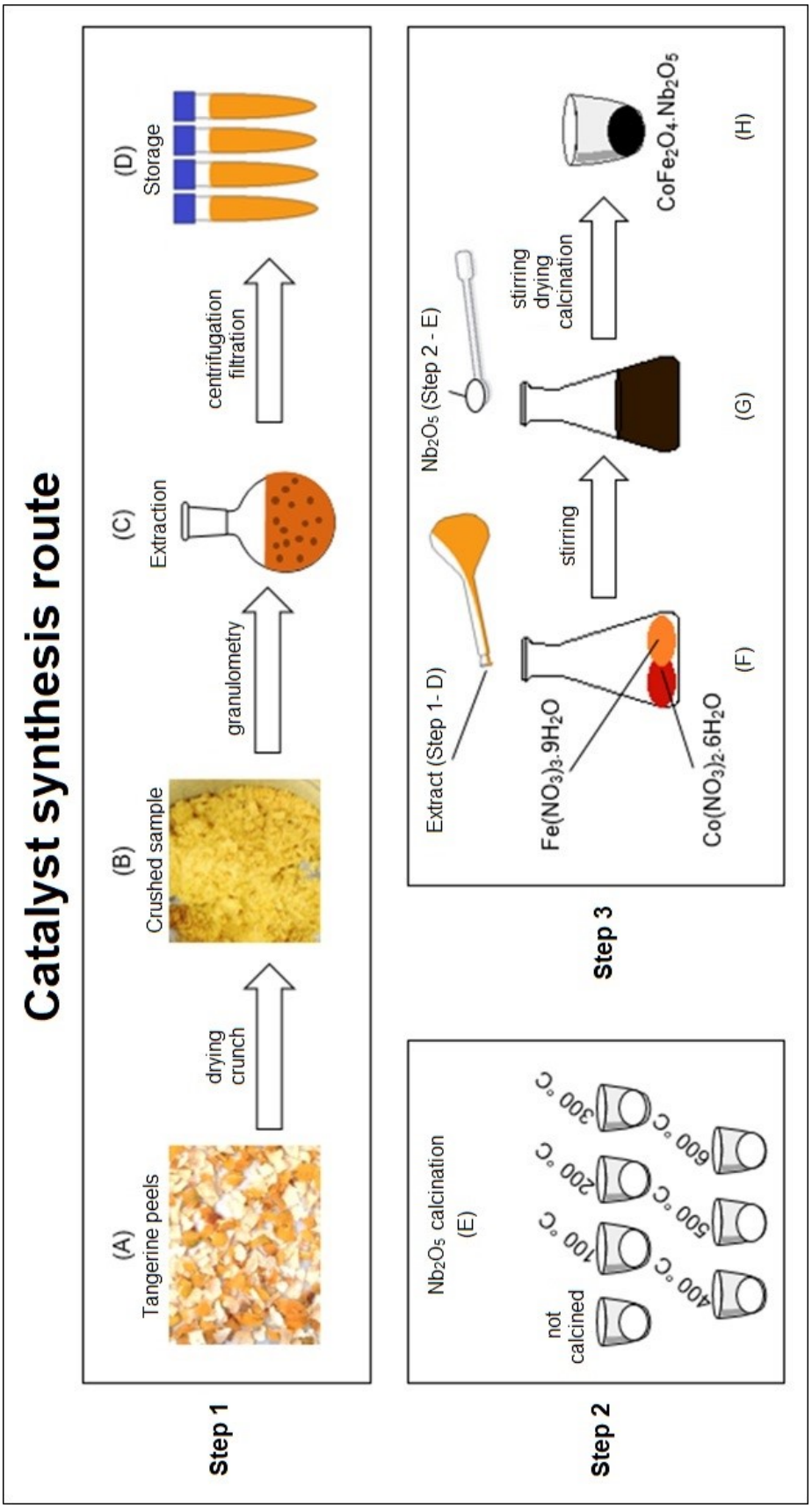

Source: own authorship

On the third step, the cobalt ferrite functionalized catalysts in niobium pentoxide ($CoFe_2O_4.Nb_2O_5$) have been synthesized. The salts Fe^{3+} (11.4 mmol) and Co^{2+} (5.7 mmol) were weighted in a 150 mL Erlenmeyer (i.e. approximately 4.61 ± 0.01 g of $Fe(NO_3)_3.9H_2O$ and 1.66 ± 0.01 g of $Co(NO_3)_2.6H_2O$). After were added 25 mL of tangerine peels extract (obtained in first step), the resultant solution showing immediately black color, Figure 4 - Step 3 (G). The Erlenmeyer was stirred in the shaker (TE-424, TECNAL) at 200 ± 2 rpm, 25 ± 2°C for 15 minutes. The theoretical weight of the cobalt ferrite to be formed was 1.33 g, so this amount of niobium pentoxide was weighted and added in the Erlenmeyer after the above referred 15 minutes, Step 3 (G). The mixture was stirred more 15 minutes under the same conditions. In sequence, the mixture was transferred to a porcelain crucible, which stayed in a drying oven for 4.5 hours at 100 ± 10 °C, until forming a gel. Finally, the porcelain crucible with the gel was placed in a calcination furnace (N1200, NOVUS) with a heating ramp as shown in Figure 5. After calcination, the resulting material in the porcelain crucible is cobalt ferrite functionalized in niobium, Figure 4 - Step 3 (H).

Figure 5 - Heating ramp used to in the synthesis of the catalysts.

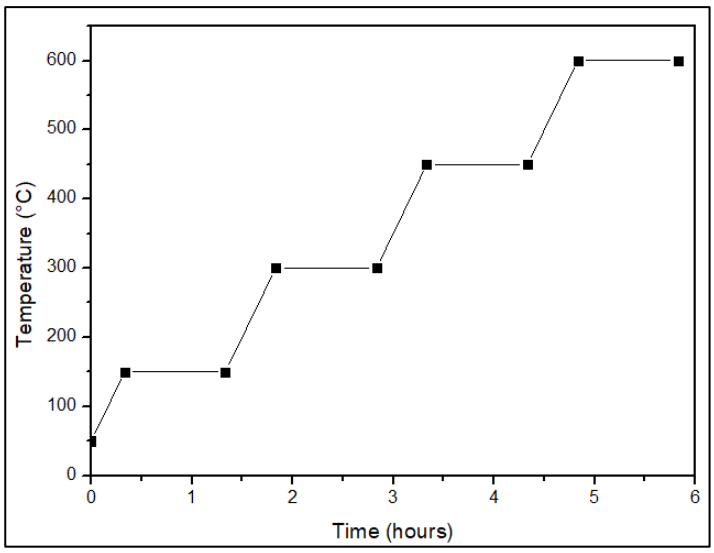

Source: own authorship

According with the calcined niobium pentoxide used the resultant materials of the Step 3 (H) were named as in the following:

- CFNb - cobalt ferrite with non-calcined niobium pentoxide;

- $CFNb_{100}$ - cobalt ferrite with niobium pentoxide calcined at 100 °C;
- $CFNb_{200}$ - cobalt ferrite with niobium pentoxide calcined at 200 °C;
- $CFNb_{300}$ - cobalt ferrite with niobium pentoxide calcined at 300 °C;
- $CFNb_{400}$ - cobalt ferrite with niobium pentoxide calcined at 400 °C;
- $CFNb_{500}$ - cobalt ferrite with niobium pentoxide calcined at 500 °C;
- $CFNb_{600}$ - cobalt ferrite with niobium pentoxide calcined at 600 °C.

In addition, other catalysts were later synthesized for comparison, namely:

- CFCANb - cobalt ferrite with commercial citric acid and non-calcined niobium pentoxide;
- CFTE - cobalt ferrite with tangerine extract, without niobium pentoxide.

4.4 CHARACTERIZATION TECHNIQUES

4.4.1 Surface and pore analyzer

The determination of the specific surface area was carried out for the characterization of porous and finely-dispersed solids (3P-INSTRUMENT, 2020). Analysis of N_2 adsorption-desorption isotherms at 77 K were carried out with a Quantachrome NOVATouch XL4 adsorption analyser to determine the textural properties of prepared samples. The BET specific surface area (S_{BET}) was calculated by the Brunauer, Emmett, Teller method (BET). The external surface area (S_{ext}) and the micropore volume (V_{mic}) were obtained by using the *t*-method and employing the ASTM standard D-6556-01 to calculate the thickness (*t*). Then, the microporous surface area (S_{mic}) was calculated subtracting the S_{ext} from S_{BET} and the average pore width (W_{mic}) by approximation ($W=4\ V_{mic} / S_{mic}$). The total pore volume (V_{Total}) was determined at p/p^0=0.98.

4.4.2 Photoacoustic spectroscopy

Photoacoustic spectroscopy is applied to measure the effect of absorbed electromagnetic energy (particularly light) by means of acoustic detection, to determine the band gap energy, relevant in photocatalysis (SHIMADZU, 2020).

Photoacoustic spectroscopy was performed at the conditions of 200-700 nm, 800 W and 23 Hz. The catalyst samples were diluted in 80% silica (quartz powder), due to the color being too dark to analyze without dilution. The evaluated catalysts were CFNb, CFNb100, CFNb200, CFNb300, CFNb400, CFNb500, CFNb600 and CFCANb, as well as Nb_2O_5 without calcination, which is an efficient photocatalyst used as a reference.

4.4.3 Point of zero charge (pHpzc)

The determination of pHpzc allows allows suppositions to be made about types of surface active centers and adsorption abilities of surfaces (POGHOSSIAN, 1997).

For this determination, approximately 0.09 g of material was added in 6 different Erlenmeyer with different initial pH values (pH_0). The Erlenmeyer flasks were loaded with 15.0 mL of 0.01 mol L^{-1} Na_2SO_4 and their pH adjusted to different values (2.0, 4.0, 6.0, 8.0, 10.0 and 12.0) using 0.02 M NaOH and 0.02 mol L^{-1} H_2SO_4 solutions. The Erlenmeyer Flasks were then placed in an orbital shaker (TE-424, TECNAL) at 200 ± 3 rpm, 25 ± 2 °C. After stirring, the suspension was separated from the catalyst by means of a magnet and the final pH was measured (pH_F). The pH of the point of zero charge was found at the intersection between the pH_0 X pH_F curve and the identity curve (SILVA, 2019).

4.4.4 Scanning Electron Microscopy (SEM)

Scanning Electron Microscopy (SEM) is employed to reveal about external morphology, chemical composition, crystalline structure and orientation of materials making up the sample (SWAPP, 2017), allowing the visualization of the structures

present in the sample or on its surface, depending on the technique used and on the characteristics of the sample (DE ASSUMPÇÃO PEREIRA-DA-SILVA; FERRI, 2017).

In addition to the image generated by SEM, another technique is widely used in conjunction with the microscope, the Energy Dispersive Spectroscopy (EDS) measurement, which allows the detection and fraction of chemical elements on the sample surface. For this analysis, an X-ray analyzer is coupled to the SEM, so that the radiation frequencies released in the X-ray spectrum are analyzed. The principle of this test is based on the analysis of photons released by the sample's atoms when the electron beam of the equipment collides with its surface. This is possible because each chemical element releases photons with specific frequencies. The results are presented in the form of an energy spectrum versus the relative peak intensity (AFINKO, 2020).

The topographic surface images were obtained using a scanning electron microscope model VEGA 3 LMU brand TESCAN, completed with a W 20 kV filament, 3.0 nm resolution, retractable SE and BSE detectors, low-vacuum mode (500 Pa) chamber with internal diameter of 230 mm and door opening of 148 mm, 5-axis compucentric stage, fully motorized, with X: 80mm, Y: 60mm and Z: 47mm movements, CCD camera for viewing the sample chamber and “chamberview” software, VegaTC operating software, data processing system and track-ball. The microscope is also equipped with a DES Detector, model AZTec Energy X-Act, resolution 130 eV, Oxford.

4.4.5 X-ray diffraction (XRD) analysis

This test serves to analyze the crystal structure and to identify and quantify the crystalline phases of the samples (PANALYTICAL, 2020). The X-ray diffractograms of the samples were obtained using a Rigaku diffractometer model Miniflex 600 with copper radiation (CuKα $\lambda = 1.54$ Å), in the Bragg angle range of $3^{\circ} \leq 2\theta \leq 90^{\circ}$, with a step of 0.05º and time fixed count of 2 seconds per step in semi-continuous mode. The signals emitted are given as an intensity graph, whose unit are expressed in counts per second (cps), as a function of the scanning angle (2θ, known as Bragg angle). To identify the materials, the signals obtained are compared with the literature in order to confirm the presence of the desired phase and / or the presence of other phases.

The average crystallite sizes (L) were calculated by Scherrer's equation (1), which is given as:

$$L = \frac{k * \lambda}{\beta * \cos\theta} \quad (1)$$

Where k is a constant equal to 0.91, λ is the wavelength of the X-ray radiation (all diffraction patterns shown in this work were performed with CuKa radiation, so λ is 0.154 nm), θ is the diffraction angle in radians and β is the full width half maximum (FWHM) in radians.

4.5 PHOTOCATALYSIS

Before tests, the calibration curve for quantification of paracetamol was charted in HPLC - High performance liquid chromatograph (YL Clarity 9100) equipped with a pre-column, C-18 column (Phenomenex) and a visible ultraviolet detector (UV-VIS) at 243 nm, which identifies itself as a peak that elutes after approximately 3.5 minutes of scanning (TAN *et al*., 2017). The mobile phase was composed of water and acetonitrile (80/20, volume ratio) with a flow rate of 1.0 mL/min. The concentration of the 20 mg L^{-1} paracetamol solution was chosen based on the literature on paracetamol degradation (RAD *et al*., 2015; VAIANO; SACCO; MATARANGOLO, 2018; BAVASSO; POGGI; PETRUCCI, 2020; MASUDI *et al*., 2020; WANG; BIAN, 2020).

All photocatalytic tests were performed in the photocatalytic chamber exemplified in Figure 6 with all elements that composite it. Therefore, the steps to carry out those tests were:

- The pH of the paracetamol solution (21.7 ± 1.9 mg L^{-1}) was adjusted with NaOH or H_2SO_4 solutions;
- The paracetamol solution was placed in the reactor (B), which was placed in the photocatalytic chamber (A);
- A jacketed reactor was used to maintain a constant temperature of approximately 25 °C. To maintain the flow of water in the reactor jacket (C1 and C2), an ultra-thermostatic bath was used (SL 152/10, SOLAB);

- Magnetic stirring (D) using magnetic stirring plate (C-MAG HS 7, IKA) (E) and constant air flow (F) started;
- The catalyst was added to the solution and samples were taken at 0, 15, 30, 45, 60, 90, 120, 180 and 240 minutes;

Figure 6 - Representation of the photocatalytic chamber and other elements for the photocatalytic reaction

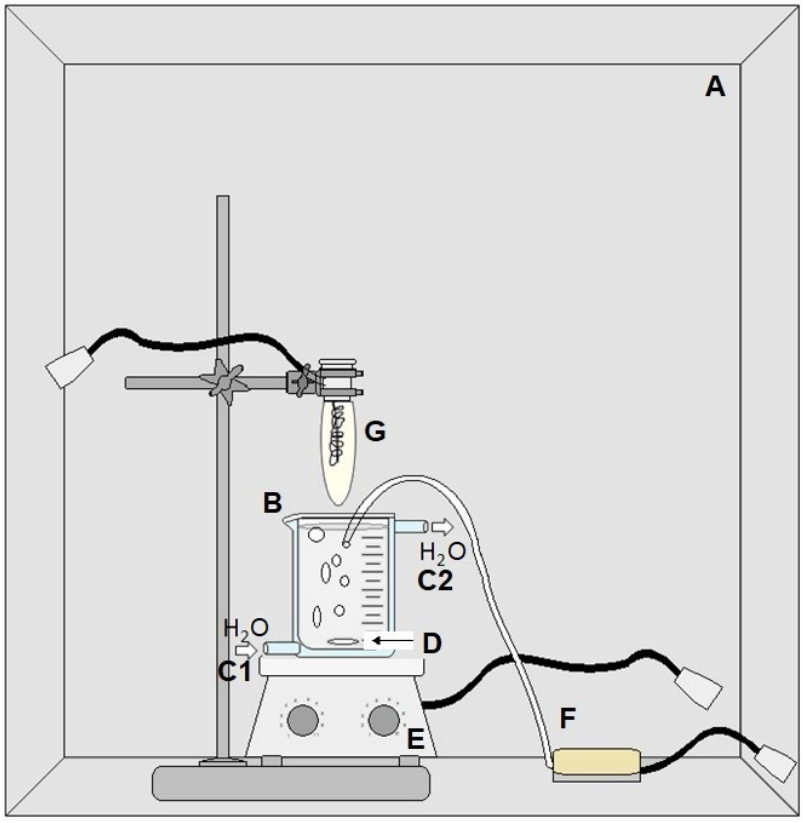

Source: own authorship

- The mercury lamp (G) was lit immediately after the sample was removed after 30 minutes of reaction, remaining on until the end of the reaction;
- All 9 samples of all reactions were analyzed using HPLC applying as a reference the calibration curve made initially.

Sequentially, was analyzed the behavior of the catalysts in photocatalysis applying preliminary tests. Parameters such as different catalysts, pH and catalyst concentration [cat] in mg L^{-1} were varied using with three factors each (minimum, maximum and central points). The preliminary tests are represented in Table 5.

Table 5 - Preliminary tests conditions.

Experiment	Catalyst	pH	[cat] - mg L^{-1}
E1	CFNb	3	300
E2	$CFNb_{600}$	3	300
E3	CFNb	9	300
E4	$CFNb_{600}$	9	300
E5	CFNb	6	100
E6	$CFNb_{600}$	6	100
E7	CFNb	6	500
E8	$CFNb_{600}$	6	500
E9	$CFNb_{300}$	3	100
E10	$CFNb_{300}$	9	100
E11	$CFNb_{300}$	3	500
E12	$CFNb_{300}$	9	500
E13	$CFNb_{300}$	6	300
E14	$CFNb_{300}$	6	300
E15	$CFNb_{300}$	6	300

Source: own authorship

After some of the preliminary experiments mentioned in Sequentially, was analyzed the behavior of the catalysts in photocatalysis applying preliminary tests. Parameters such as different catalysts, pH and catalyst concentration [cat] in mg L^{-1} were varied using with three factors each (minimum, maximum and central points). The preliminary tests are represented in Table 5.

Table 5, a Design of Experiments (DOE) was planned. This time, minimum and maximum points of three factors were studied, with one repetition, resulting in eight tests. In this DOE just CFNb catalyst was used and the different parameters explored were pH, lamp power (watts, W) and catalyst concentration (mg L^{-1}), as shown in Table 6. However, this time, formic acid was used to adjust the pH and also as an additive to

improve the performance of the catalyst, and the paracetamol solution concentration was 21.7 ± 1.9 ppm.

After the results of the DOE, the conditions to obtain the best results were identified and called the "6B" experiment. Which was used to evaluate the efficiency of the other catalysts mentioned, as well as tests for reuse, adsorption, photolysis, long-time test and sky open photocatalysis test (solar radiation).

Table 6 - Design of Experiments 2^3.

Experiment	**pH**	**Lamp power**	**[cat] - mg L^{-1}**
1A	2	125W	300
2A	9	125W	300
3A	2	125W	100
4A	9	125W	100
1B	2	250W	300
2B	9	250W	300
3B	2	250W	100
4B	9	250W	100

Source: own authorship

5 RESULTS AND DISCUSSION

5.1 SYNTHESIS OF COBALT FERRITE FUNCTIONALIZED IN NIOBIUM PENTOXIDE

For the synthesis of cobalt ferrite, the obtention of tangerine extract is a crucial step (step 1), in which all details are important for the process, seeking the best performance of the materials. Kiln drying (A) helps to eliminate many of the microorganisms, avoiding rotting of the peels and facilitating grinding in an analytical mill (B). The grinding together with the granulometry allows to obtain a more uniform powder of the peels, making better use of them at the time of extraction, so that there is a good process repeatability. It was chosen to do the extraction with water (C) to eliminate the use of toxic solvents, and this was an efficient solvent to extract the components necessary for the synthesis. The extraction was followed by centrifugation and filtration to obtain the extract as clear as possible to use it (D).

A triplicate test was performed to titrate the tangerine extract obtained in step 3 (D), in order to know the acid content contained in the obtained extract. For this, 2 drops of phenolphthalein were added to 5.0 mL of extract without dilution in an Erlenmeyer flask and a burette was filled with a standardized solution of NaOH 1.0 mol L^{-1}. NaOH was added dropwise to the phenolphthalein containing extract solution and 0.8 , 0.8 and 0.7 mL of NaOH solution were spent to titrate samples 1, 2 and 3 respectively, resulting in a mean of 0.767 mL of NaOH. As citric acid ($C_6H_8O_7$) is a carboxylic acid, it has three dissociable hydrogens (3 H^+) in the carboxylic acid groups, as shown in Figure 7, and considering that the acid from the extract was only citric acid, the molar concentration of citric acid (M_A) in the extract was calculated, M_A equal to 0.046 mol L^{-1}.

Figure 7 - Structure of citric acid and different acid dissociation constants (pKa)

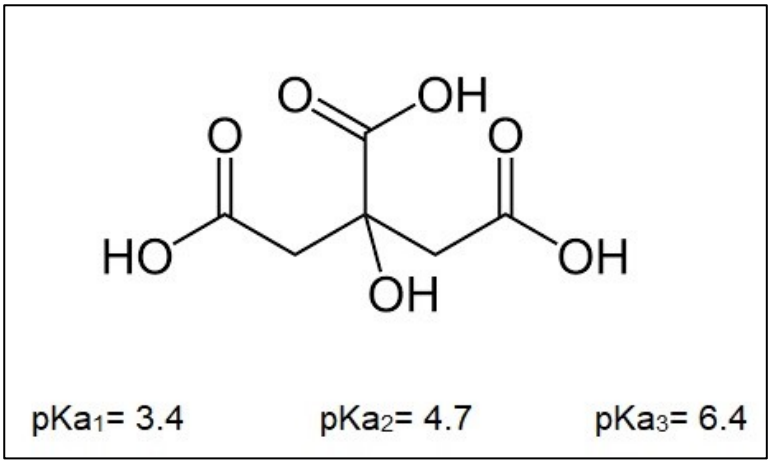

Source: (SALIHU *et al*., 2021), adapted.

The determination of the acid concentration of the extract was used to calculate how much commercial citric acid should be used to prepare the CFCANb catalyst, to serve as comparison, and which was used with a molar concentration of 0.05 mol L^{-1}.

In step 2, the intention of testing different calcination temperatures of Nb_2O_5 (E) before adding it to the synthesis of the NMs is to assess the influence of the change in the structure of niobium (amorphous, pseudo-hexagonal or orthorhombic) on the different catalysts obtained in relation to their structures, magnetism, surface contact and activity, among other characteristics. However, it is also important to note that after the addition of Nb_2O_5 to the mixture of Fe^{3+} and Co^{2+} salts with the tangerine extract (step 3 - G), an heat treatment up to 600 °C is also performed, which can also alter the structure of the Nb_2O_5 obtained in step 2 (E) and approximate the structural and behavioral characteristics of the resulting NMs at the end of the synthesis.

Given the above, this evaluation around the differences in catalysts as a function of the heat treatment of niobium pentoxide can only be conclusive by comparing the characterizations and the result of their applications in the photocatalytic reactions.

In step 3, the mixture of the salts with the extract followed by stirring before adding niobium pentoxide (F) was done aiming to form cobalt ferrite that in later processes would be deposited on the surface of Nb_2O_5. The addition of this support in step (G) followed by agitation was carried out with the goal to distribute homogeneously the cobalt ferrite throughout the resulting catalyst after step 3 (H). Kiln drying was carried out aiming to form a gel prior to calcination, this gel formation preventing the catalyst from spilling into the muffle, since if it were suddenly subjected to high temperatures, it could boil and would lose all material.

After completing the synthesis of the materials, in the recovery of the material that remains in the porcelain crucible after calcination, step 3 (H), there is a weight loss around 11 ± 3%, Figure 8. The catalysts were stored in Falcon tubes until use and the magnetic properties were tested by approaching a magnet. As shown in Figure 9, the magnet is able to hold the tube containing the sample, as the magnetic attraction is very strong.

Figure 8 - Catalyst recovered for storage after completing step 3 (H).

Source: own authorship

Figure 9 - Demonstration of the magnetic properties. All material, including the Falcon tube, is supported by a magnet.

Source: own authorship

Besides the magnetic properties, that facilitates the separation after using the NMs in reactions, the type of synthesis created has several advantages over other types of synthesis already reported in literature. Among the advantages can be highlighted:

• Utilization of biomass, namely fruit peels, which would be destined for common waste or as compost;

• Extract production using only distilled water as a solvent and low temperatures;

• High yield in the production of NMs, about 3.0 g of cobalt ferrite functionalized in niobium pentoxide are obtained with 1.0 g of dried fruit peels;

• With the yield mentioned (3 g/g of dried fruit peels), it suggests a possible large-scale production;

• Incorporation of the niobium pentoxide support in the same stage of synthesis of cobalt ferrite, when most other methods first suggest the synthesis of the precursor and then impregnation in the support, which would require more time and higher cost;

• High support incorporation compared to other methods, without losing or decreasing the magnetic properties of cobalt ferrite;

• Added-value to a raw material abundant in Brazilian territory, niobium;

• Low cost synthesis, using common equipments of laboratory, and relatively low cost.

5.2 CHARACTERIZATION

5.2.1 BET surface area

The textural properties of the Nb_2O_5 samples, obtained by calcination at different temperatures, step 2 (E) of the synthesis, were determined and the results shown in Table 7.

Table 7 - Results of BET surface area of the calcined niobium pentoxide samples.

Samples	S_{BET} (m^2/g)	Sext (m^2/g)	Smic (m^2/g)	Vmic (mm^3/g)	Vtotal (mm^3/g)
Nb	185	88	97	50.3	158
Nb100	178	103	75	39	163
Nb200	156	113	43	22.7	160
Nb300	134	106	28	14.5	145.1
Nb400	112	103	9	5.3	131.4
Nb500	69	69	0	0	118
Nb600	31	31	0	0	99.1

Source: own authorship

Evaluating the data given in Table 7 it is possible to conclude that S_{BET}, S_{mic} and V_{mic} decreases as the calcination temperature of Nb_2O_5 increases. The change in these

values is related to the structure of Nb_2O_5, which, as already mentioned, is amorphous until heat treatment at 400 °C and, therefore, must have presented higher values up to this temperature. For temperatures above 500 °C the material may have been sintered, to form the pseudohexagonal and orthorhombic structures, or still if crowded decreasing the S_{BET} values, as shown in Table 7 .

In theory, it would be more interesting to use the material with higher S_{BET}, S_{mic} and V_{mic}, as it would better aggregate the cobalt ferrite (CF) particles and still have a higher surface area for active sites for catalysis. However, after mixing with the Fe^{3+} and Co^{2+} salts reagents and tangerine extract, there is another heat treatment step up to 600 °C, and this temperature may also influence the behavior of both the Nb_2O_5 and the final catalyst. In addition, it should be also taken into consideration the structure of Nb_2O_5, if was amorphous, pseudohexagonal, hexagonal or orthorhombic, which for application in photocatalysis may have great influence.

According to the literature, the materials containing niobium pentoxide and cobalt ferrite have specific surface area BET (S_{BET}) according to the values mentioned in Table 8. However, there is not specific comparison for the material $CoFe_2O_4@Nb_2O_5$, as it is an innovation.

In general, it is possible to conclude that as calcination temperature of Nb_2O_5 increases the value for S_{BET} decreases. And when niobium supports some metal, these values will depend on both the metal content and the calcination temperature. The $CoFe_2O_4$ have low S_{BET} values, however if supported on a highly porous material (such as graphite) it can increase the S_{BET} value, as observed in Table 8.

Table 8 - S_{BET} values reported in the literature for Nb_2O_5 and $CoFe_2O_4$ compounds

Material	SBET (m²/g)	T calcination	Reference
Nb_2O_5	24	500 °C	(SILVA *et al*., 2002)
Nb_2O_5	81 ± 8	100 °C	(FALK *et al*., 2017)
	36 ± 4	500 °C	
	22 ± 2	600 °C	
	13 ± 1	800 °C	
Amorphous-Nb_2O_5	129.6	450 °C	(LI *et al*., 2016)
Pseudohexagonal-Nb_2O_5	57.8	600 °C	
Orthorhombic-Nb_2O_5	43.0	800 °C	
Nb_2O_5/C nanocomposites	98.33	600 °C	(ZENG *et al*., 2017)
Fe/Nb_2O_5			(FIDELIS *et al*., 2019)
0.5% Fe	20.26	400 °C	
1.5% Fe	64.90	400 °C	
0.3% Fe	43.44	500 °C	
1.0% Fe	149.63	500 °C	
1.7% Fe	43.44	500 °C	
0.5% Fe	148.83	600°C	
1.5% Fe	21.24	600°C	
Cobalt ferrite core and a graphitic shell	330	500 °C	(RIBEIRO *et al*., 2019)
$CoFe_2O_4$	44	400 °C	(IANOȘ, 2014)

Source: own authorship

Figure 10 shows the comparison of all the adsorption isotherms for the samples of niobium pentoxide calcined up to 600 °C. To characterize the catalysts in terms of the type of material, the IUPAC (International Union of Pure and Applied Chemistry) provides a classification for physisorption isotherms and associated hysteresis loops (THOMMES *et al*., 2015), shown in

Figure 11 and Figure 12, respectively.

Figure 10 - Adsorption isotherms for calcined niobium pentoxide samples.

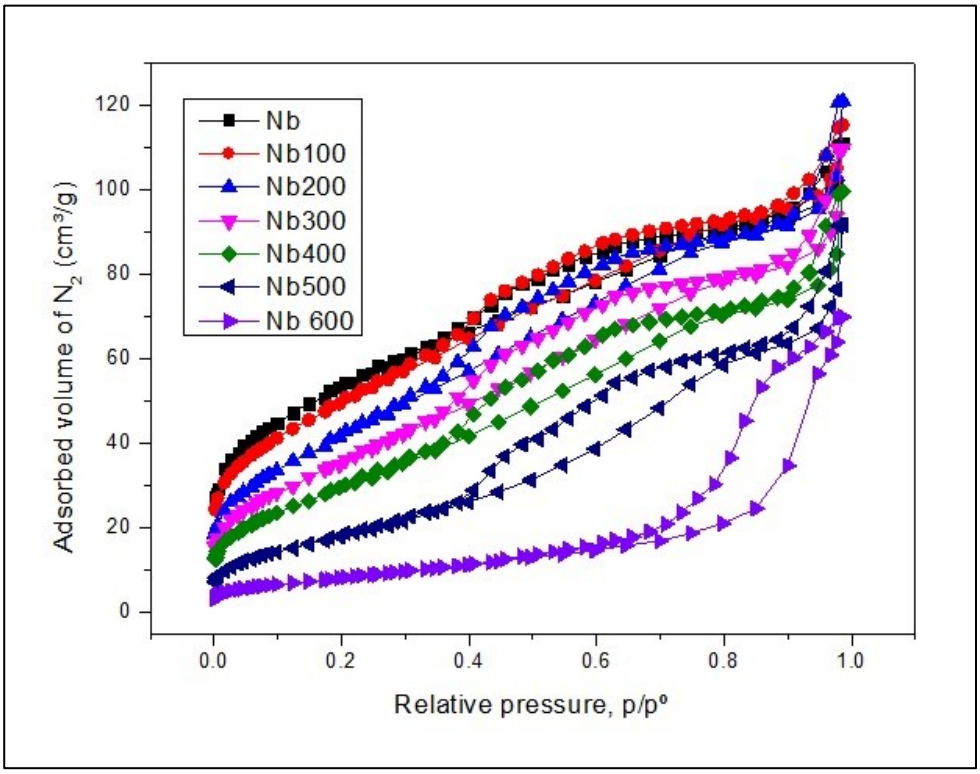

Source: own authorship

Figure 11 - Classification of physisorption isotherms by IUPAC.

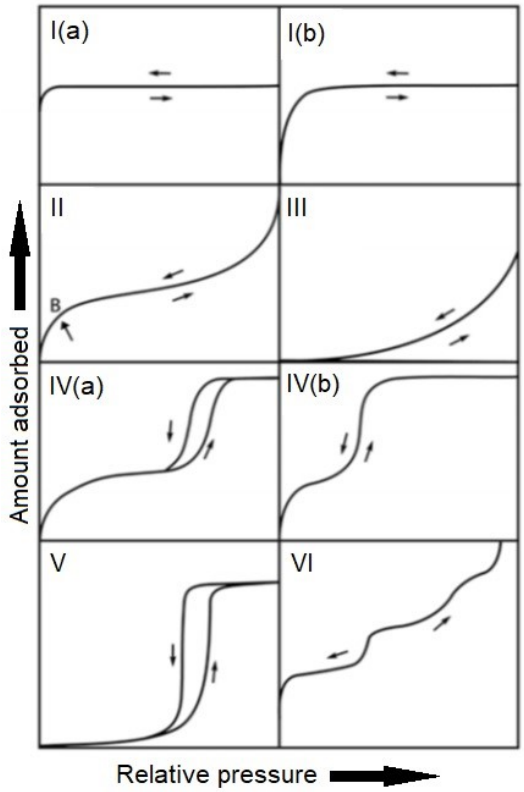

Source: (THOMMES *et al.*, 2015), adapted.

Figure 12 - Classification of hysteresis loops by IUPAC.

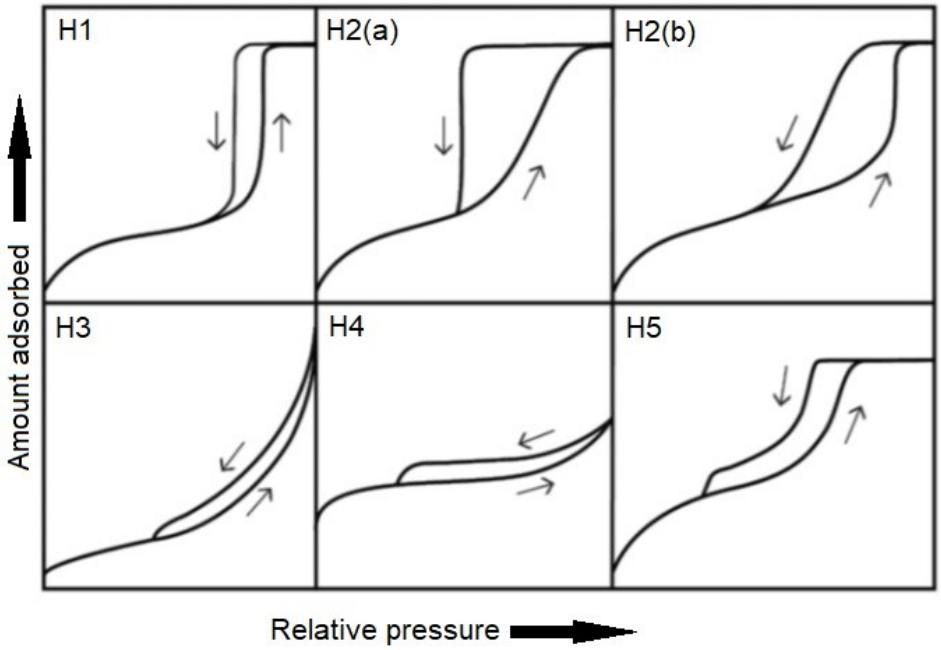

Source: (THOMMES *et al*., 2015), adapted.

According to the IUPAC classification (Figure 11 and 12) for physisorption isotherms and associated hysteresis loops and the hysteresis loop, the Nb_2O_5 calcined up to 500 °C (graphs Nb, Nb100, Nb200, Nb300, Nb400 and Nb500) are IVa - H4 and the Nb_2O_5 calcined at 600 °C (Nb600) are IVa-H5.

5.2.2 Photoacoustic spectroscopy

The photoacoustic spectrum (PAS) in the UV-Vis region of 200-700 nm for the catalysts showed a broad absorption band between 225−420 nm similar to the PA spectrum of non-calcined Nb_2O_5,

Figure 13. Applying the photoacoustic method with phase resolution (PRPA) to the non-calcined Nb_2O_5 spectrum, an average phase difference of (12 ± 3)° was observed between two different absorption peaks. Therefore, the PRPA method indicated two absorber centers in the region between 225-420 nm. The PRPA method found an absorption peak at 300 nm (peak 1), corresponding to the transition from ligand to metal charge transfer (LMCT) from O^{2-} to Nb^{5+}, and another at around 450 nm (peak 2) due to niobium nanodomains (probably corner sharing NbO_6 octahedron).

For all catalysts, peak 1 remained at approximately 300 nm, however peak 2 shifted to blue around 50 nm compared to non-calcined Nb_2O_5, Figure 14 .

The intensity of the photoacoustic signal did not change with increasing calcination temperature during the synthesis. This result, in addition to not indicating changes in the band gap and in the absorption threshold, suggests little variation in the size of the crystal with the increase of the calcination temperature.

Figure 13 - Photoacoustic absorption spectrums, 200-700 nm, 800 W, 23 Hz for non-calcined Nb_2O_5.

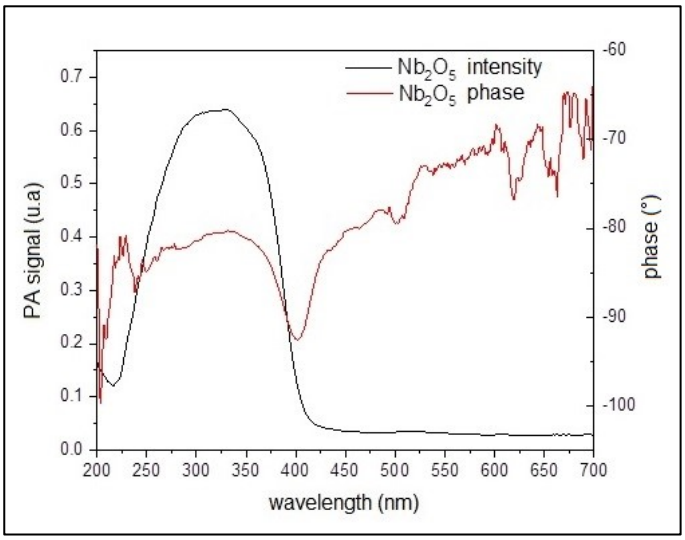

Source: own authorship

Figure 14 - Photoacoustic absorption spectrums, 200-700 nm, 800 W, 23 Hz for catalyst samples.

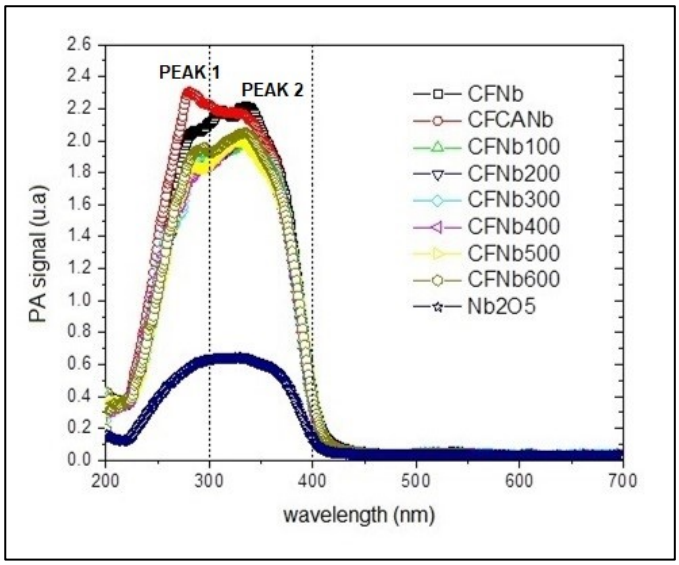

Source: own authorship

The GAP energy was calculated using the linear method and the derivative method, according to

Figure 15 A and B, respectively. Since there was no significant variation with the increase in Nb_2O_5 calcination before the synthesis of the material, it can be said that it was an average value very close to the value of the gap energy for Nb_2O_5 recorded in the literature, equal 3.1 (GREENWOOD; EARNSHAW, 1997). The GAP energy values are shown in Table 9. For the linear method, equation (2) was used:

$$\left(a(h\nu)\right)^2 = A\left(h\nu - E_g\right) \qquad (2)$$

Figure 15 - Band-gap energy for the CFNb sample. A: using the linear method. B: using the derivative method.

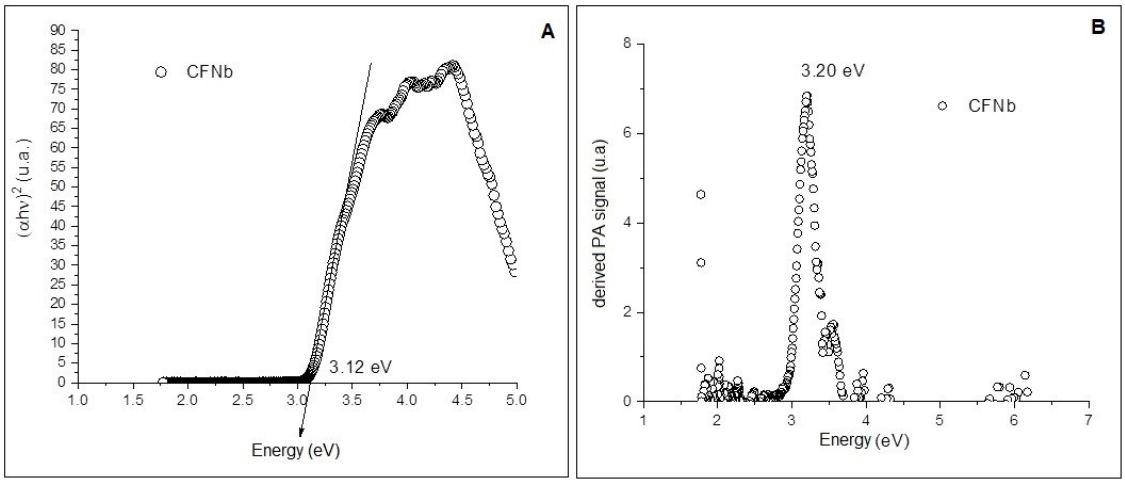

Source: own authorship

Table 9 - Band-gap energy of the catalyst samples, using both methods: linear and derivative

Samples	Eg (eV) linear method	Eg (eV) derivative method
CFNb	3.12	3.20
CFCANb	3.13	3.19
CFNb100	3.12	3.20
CFNb200	3.13	3.19
CFNb300	3.13	3.20
CFNb400	3.15	3.20
CFNb500	3.14	3.19
CFNb600	3.16	3.20
Nb_2O_5	3.14	3.19

Source: own authorship

As mentioned, the band gap value for Nb_2O in the literature is 3.1 eV, while for cobalt ferrite around 1.1 eV (CHAVARRIAGA *et al*., 2020). Thus, it is observed that niobium pentoxide has more influence on this characteristic of the nanomaterial than the metal complex. To compare niobium pentoxide with different iron fractions, the band gap ranges from 3.05 to 3.94 eV, with values relatively close to those found in this work (FIDELIS *et al*., 2019). In comparison with TiO_2 P25, the most widely used commercial photocatalyst, it has a band gap equal to 3.2 eV (NÚÑEZ *et al*., 2021). The fact that the synthesized catalysts have a band gap close to that of TiO_2 P25, reveals that they may be also promising for application in photocatalysis.

5.2.3 Point of zero charge (pHpzc)

Depending on the pH, the catalyst surface may be uncharged, negatively or positively charged. The isoelectric point, also known as PZC (point of zero charge), is the pH at which the suspended particles have zero net charge and no mobility in the electric field (pH_{PZC}) (FARAJI; YAMINI; REZAEE, 2010). Following the procedure described in the methodology, the pH_{PZC} was obtained by intercepting the experimental curves of each sample with the identity curve.

Among the evaluated catalyst samples, two curve profiles for pH_{PZC} were presented around pH 4.0, which were separated in graphs A and B of

Figure 16. However, both profiles showed neutral and similar pH_{PZC} between 6 and 7.5, according to Table 10.

Figure 16 - pH_{PZC} curves of the tested materials.

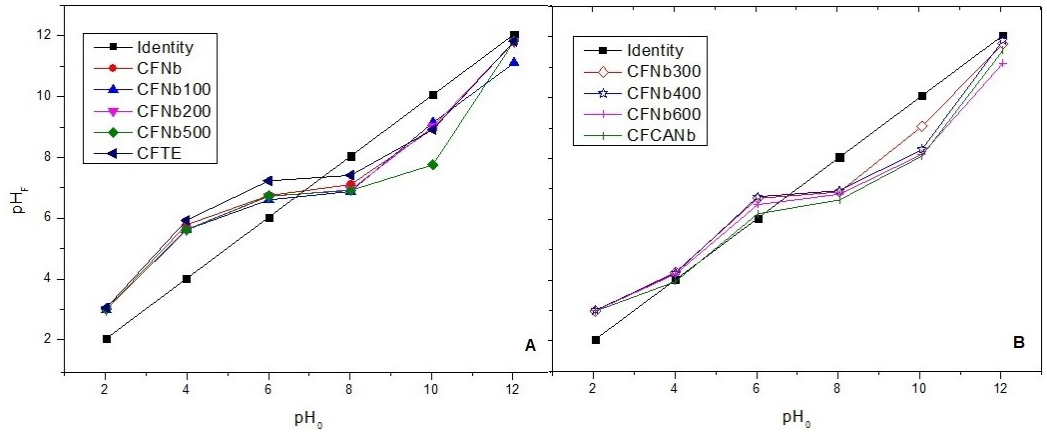

Source: own authorship

Table 10 - pH_{PZC} values calculated by the intersection of the curves represented in Figure 16.

Samples	pH_{PZC}
CFNb	6.9
CFNb100	6.7
CFNb200	6.8
CFNb300	6.8
CFNb400	6.8
CFNb500	6.8
CFNb600	6.6
CFCANb	6.2
CFTE	7.4
Mean ± sd	6.8 ± 0.3

Source: own authorship

From the results of pH_{PZC} it is possible to notice that when the cobalt ferrite was produced without the addition of niobium (CFTE) it presented a pH_{PZC} value slightly higher than the other values. In addition, comparing CFCANb with CFNb, the first one that was synthesized with commercial citric acid showed a slightly lower pH_{PZC} value, in relation even with the other samples synthesized with the extract of the tangerine peels, suggesting that the extract gave to the synthesized material some particularity in its structure.

5.2.4 Scanning Electron Microscopy (SEM)

The working principle of the SEM is related to an interaction between electrons and matter. The Scanning Electron microscope contains a source that generates an electron beam that is continuously fired in the sample during the test, scanning its surface. Thus, through a detector present in the equipment, it is possible to analyze the electron energies during an interaction between them and the surface, which are interpreted by the equipment and generate images like as in Figure 17, representing

the characterization of the samples CFNb, $CFNb_{100}$, $CFNb_{200}$, $CFNb_{300}$, $CFNb_{400}$, $CFNb_{500}$, $CFNb_{600}$ and CFCANb. It is possible to observe clusters of nanomaterials, very typical of materials that have magnetic properties (HUANG *et al*., 2014; MAKAROV *et al*., 2014; HARSHINY; ISWARYA; MATHESWARAN, 2015; MACHADO *et al*., 2015; SONU *et al*., 2019; SHI *et al*., 2020). In addition, it is possible to observe the surface difference of the CFCANb sample, which was produced with commercial citric acid instead with the tangerine extract. It apparently has a planar surface, possibly because it formed larger clusters (in blocks). In contrast, the other samples could still be divided into two groups due to apparent small superficial similarity, on the one hand CFNb, $CFNb_{100}$, $CFNb_{200}$ and $CFNb_{300}$ and on the other $CFNb_{400}$, $CFNb_{500}$ and $CFNb_{600}$. This may be related to the calcination temperature of Nb_2O_5 before synthesis.

Figure 17 - SEM images of the samples.

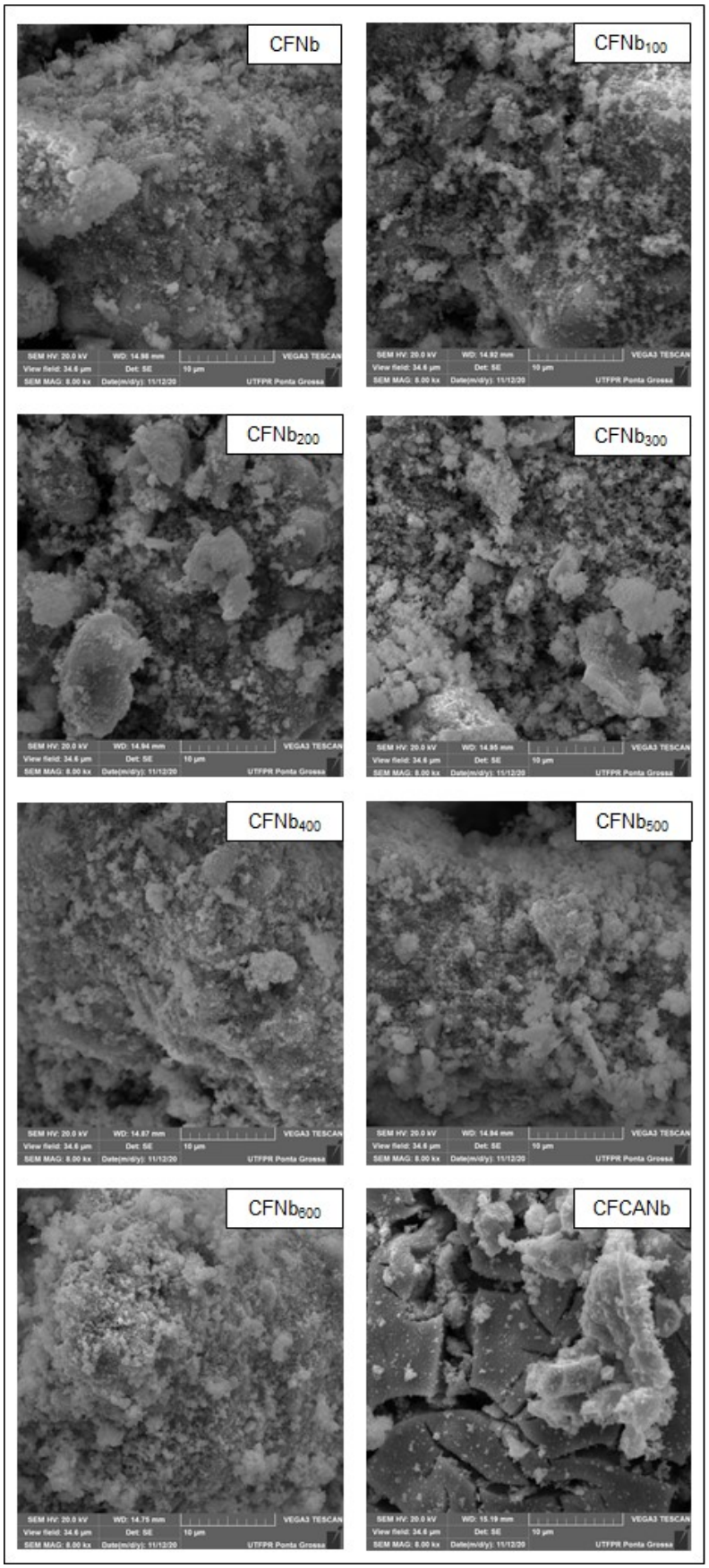

Source: own authorship

Energy Dispersive Spectroscopy (EDS), which allows the detection and fraction of chemical elements of chemical elements on the surface, was performed for catalysts CFNb, $CFNb_{100}$, $CFNb_{200}$, $CFNb_{300}$, $CFNb_{200}$, $CFNb_{300}$, $CFNb_{400}$, $CFNb_{500}$ and $CFNb_{600}$. The fraction of each component is summarized in the

Table 11, as well as the mean and standard deviation per component.

Table 11 - Components percentage in weight, resulting from EDS analysis.

	CFNb	CFNb100	CFNb200	CFNb300	CFNb400	CFNb500	CFNb600	Mean ± sd
O (W %)	33.6	35.7	32.7	30.2	31.1	31.6	27.8	31.8 ± 2.5
Fe (W %)	27.3	26.6	24.4	31.6	27.8	34.7	42.9	30.8 ± 6.4
Nb (W %)	24.8	27.2	32.0	15.9	25.8	17.7	14.3	22.5 ± 6.6
Co (W %)	14.0	10.3	10.9	22.2	15.3	15.8	14.7	14.7 ± 3.9

Source: own authorship

It should be bear in mind that it was expected to obtain the synthesis of nanomaterials of functionalized cobalt ferrite in niobium pentoxide of supposed molecular formula $CoFe_2O_4@Nb_2O_5$ and that the atomic weight of one mole of this component would be about 500.44 u (assuming Co = 58.93 u, Fe = 55.845 u, O = 16 u and Nb = 92.91 u). Recalling that the synthesis was performed with 50% w/w of $CoFe_2O_4$ and Nb_2O_5, the theoretical fraction by weight of each element would be O = 28.68± 0.00%, Fe = 23.92 ± 0.02%, Nb = 34.78 ± 0.04% and Co = 12.62 ± 0.01%. These values are considered close to the values obtained considering the standard deviation for more and for less, therefore, it can be considered that $CoFe_2O_4@Nb_2O_5$ was really the synthesized material.

The images that demonstrate the SEM/EDS characterization with the separation analysis by component are in APPENDIX A. For the sake of curiosity, complementary information is found from

Figure 30 to

Figure 36.

5.2.5 X-ray diffraction (XRD) analysis

The interpretation of the XRD analysis of the synthesized samples were done using the standards published by the Joint Committee on Powder Diffraction Standards - International Center for Diffraction Data (JCPDS - ICDD) cards No. 22-1086, No.28-0317 and No.30-0873 that concern cobalt ferrite, pseudo-hexagonal phase (TT-Nb_2O_5) and orthorhombic phase (T-Nb_2O_5) of niobium pentoxide, respectively.

According to the aforementioned standards (Figure 18), which belong to face-centered cubic spinel type (Fd - 3m), the cobalt ferrite has an estimated lattice parameter a = b = c = 8.38 Å. In addition, this compound is characterized by having peaks between 2Θ° = 15° and 70° as follows: 18.289°, 30.085°, 35.438°, 37.057°, 43.059°, 53.446°, 56.975°, 62.587°, which correspond to the indices of Miller (111), (220), (311), (222), (400), (422), (511) and (440), respectively (SAJJIA *et al*., 2010; LONG *et al*., 2015; PURNAMA; WIJAYANTA; SUHARYANA, 2019).

On the other hand, the pseudo-hexagonal and orthorhombic phases of niobium pentoxide have very similar patterns,

Figure 19. The TT-Nb_2O_5 (JCPDS - ICDD 28-0317), with lattice parameters a = 3.607 Å, b = 3.607 Å, c = 3.925 Å; space group: P6/mmm, has the Miller indices (001), (100), (101), (002), (110), (102) and (112) (LIU; XUE, 2010; HE *et al*., 2014; MORAWA EBLAGON *et al*., 2020). The T-Nb2O5 (JCPDS - ICDD 30-0873), with lattice parameters a = 6,175 Å, b = 29,175 Å, c = 3,930 Å and space group: Pbam, has typical diffraction peaks located at 22.7°, 28.5°, 36.7°, 46.2°, 50.6°, 55.1° and 71.0°, which correspond to the Miller indices (001), (180) , (181), (002), (380), (182) and (382), respectively (ZENG *et al*., 2017; LIAO *et al*., 2018; SEO; KIM; KIM, 2020).

Figure 18 - Standard X-ray diffractogram of cobalt ferrite

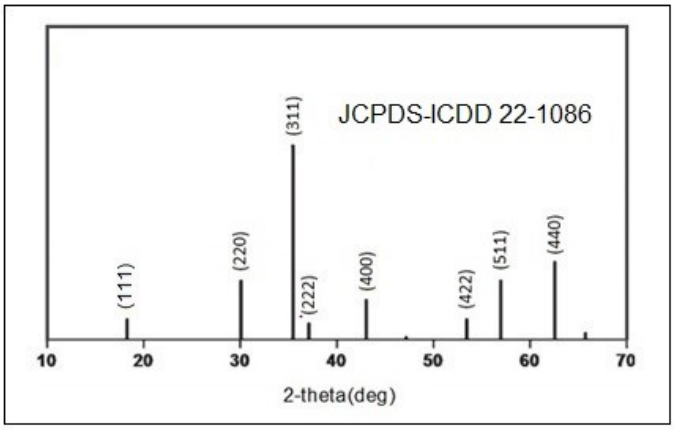

Source: (SAJJIA *et al*., 2010; LONG *et al*., 2015; PURNAMA; WIJAYANTA; SUHARYANA, 2019), adapted.

Figure 19 - Standard X-ray diffractogram of the TT-Nb_2O_5 (JCPDS - ICDD No. 28-0317) and T-Nb2O5 (JCPDS - ICDD No. 30-0873).

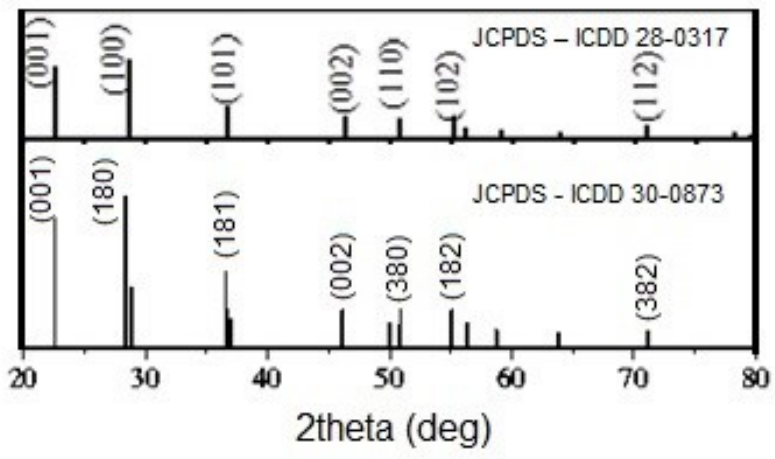

Source: (ZENG *et al*., 2017; LIAO *et al*., 2018; MORAWA EBLAGON *et al*., 2020), adapted.

Figure 20 shows the X-ray diffractograms obtained for the samples CFNb, $CFNb_{100}$, $CFNb_{200}$, $CFNb_{300}$, $CFNb_{400}$, $CFNb_{500}$, $CFNb_{600}$ and CFCANb. In this figure, the peaks related to ferrite were identified as cobalt and niobium pentoxide, represented by the acronyms CF and Nb, respectively. Comparing the patterns with the obtained results, it is observed that all samples have peaks in the diffraction angles for the mentioned components. Identifying the cobalt ferrite, the peaks appear around 2theta angles of 18.3°, 30.3°, 35.5°, 37.1°, 43.1°, 53.5° and 62.6°, corresponding to the mentioned pattern. For the identification of niobium pentoxide, it was observed

peaks for the 2theta angles of 22.6°, 28.4°, 36.4°, 46.2°, 50.2°, 55.2° and 71.1°, which correspond to the aforementioned patterns. By this way it is possible to identify that the obtained samples refer to the material of cobalt ferrite functionalized in niobium pentoxide.

Furthermore, it is possible to observe some details, such as the increase in intensity around the angles 2theta of 46.2°, 55.2° and 71.1°, which increase as the Nb_2O_5 calcination temperature increases in step 2 of the synthesis, being more intense for temperatures between 400 and 600 °C. This difference is possibly related to the structure of niobium pentoxide in the material.

Figure 20 - Components identification in the diffractogram (cobalt ferrite = CF; niobium pentoxide = Nb)

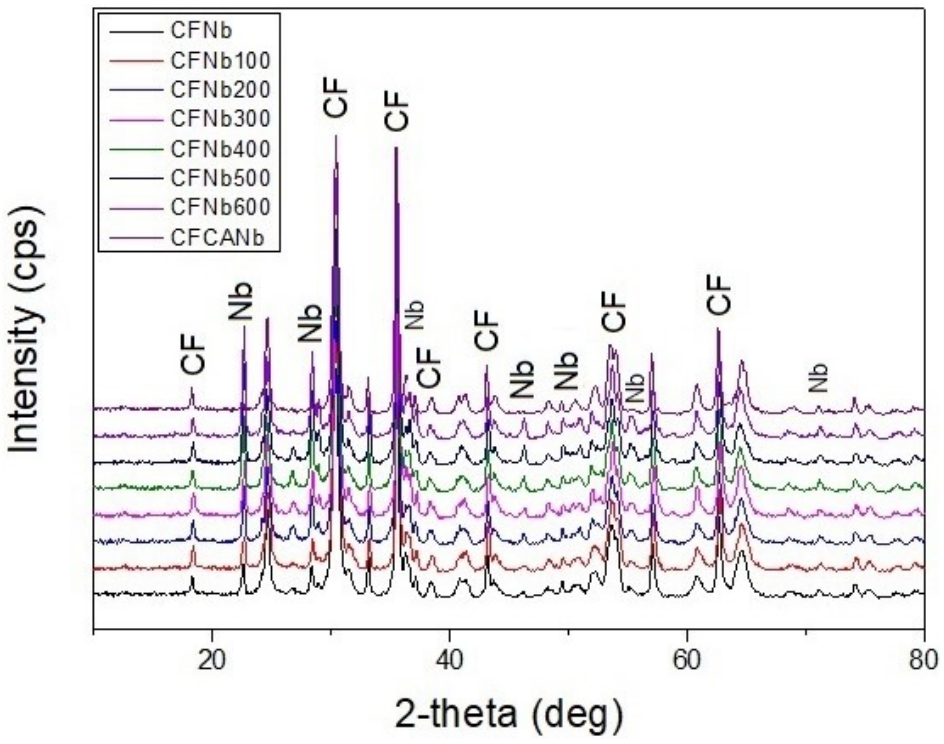

Source: own authorship

One way to better define the structure obtained is by using a characterization refinement to compare lattice parameters, which for each structure has its specificity. Another way is to manually calculate the lattice parameter (a) using the classical formula given by equation (3) (YAKUBU *et al*., 2015).

$$\frac{1}{d^2} = \frac{h^2 + k^2 + l^2}{a^2} \quad (3)$$

where h, k and l are parameters related to the Miller index of the structure (i.e. (180), so h is 1, k is 8 and l is 0); d is the distance between one plane and the other, which can be calculated by the Bragg's law, equation (4).

$$2d \sin\theta = n\lambda \quad (4)$$

where λ is the wavelength of the X-ray radiation (all diffraction patterns shown in this work were performed with CuKa radiation, so λ is 0.154 nm or 1.54 Å); θ is the diffraction angle in radians; and n is constructive interference (n=1,2,3,...,n). Substituting equation (3) on equation (4), equation (5) is obtained.

$$a = \lambda \frac{[h^2 + k^2 + l^2]^{1/2}}{2 \sin\theta} \quad (5)$$

The values of the calculated lattice parameters were tabulated for better comparison with the values established by the cited standards,

Table 12. It can be observed that the values of the lattice parameters for cobalt ferrite were very close to the values established as standard. As for niobium pentoxide, the values were closer to TT-Nb_2O_5 than to T-Nb_2O_5, which concerns the pseudo-hexagonal phase, which is possibly the predominant phase in the material obtained.

Table 12 - Results of the lattice parameters.

Sample	$CoFe_2O_4$ (a=8.38 Á)	TT-Nb_2O_5 (a=3.61 Å)	T-Nb_2O_5 (b=29,17 Å)
CFNb	8.38	3.53	25.38
CFNb100	8.36	3.51	25.31
CFNb200	8.37	3.52	25.40
CFNb300	8.37	3.51	25.31
CFNb400	8.37	3.53	25.35
CFNb500	8.37	3.51	25.32
CFNb600	8.36	3.51	25.35

CFCANb	8.37	3.03	20.10

Source: own authorship

Further exploring the results of the XRD characterization, the average crystallite sizes (L) were calculated using the Scherrer's equation (1) mentioned in section 4.4.5, the results are shown in Table 13. It is possible to observe that the thermal treatment of niobium (step 2) did not significantly influence the average crystallite sizes of the material. As a general rule, the higher the temperature, the larger the crystallite size. The material with the largest average crystallite size (33.85 nm) was synthesized with commercial citric acid, instead of tangerine extract (CFCANb).

Table 13 - The average sizes of crystallites (D), calculated using the Scherrer's equation.

Samples	L (nm)
CFNb	24.10
CFNb100	22.78
CFNb200	25.39
CFNb300	24.82
CFNb400	26.34
CFNb500	27.36
CFNb600	28.13
CFCANb	33.85

Source: own authorship

Evaluating the characterizations as a whole, it is possible to conclude that the thermal treatment (step 2) was not so impacting in the formation of the catalysts and only small differences are noticed, all samples being cobalt ferrite functionalized in niobium pentoxide as predicted ($CoFe_2O_4@Nb_2O_5$).

5.3 PHOTOCATALYSIS

Before the photocatalytic runs with the synthesized materials, a calibration curve to quantify the concentration of paracetamol (PCT) during the course of the reactions was performed. HPLC was used as analytical technique and concentrations between 0.7 and 50 ppm were considered. The calibration curve resulted in the linear equation y=85.326*x+42.425 show in

Figure 21, with R^2 equal to 0.997, where x is the area in mV.s (miliVolt.second) and y is the concentration of PCT in mg L^{-1}. All samples collected during the various photocatalytic experiments were read on the HPLC equipment, as mentioned in the methodology, and compared with the PCT calibration curve to determine the corresponding PCT concentration.

Figure 21 - Calibration curve of the Paracetamol in the HPLC.

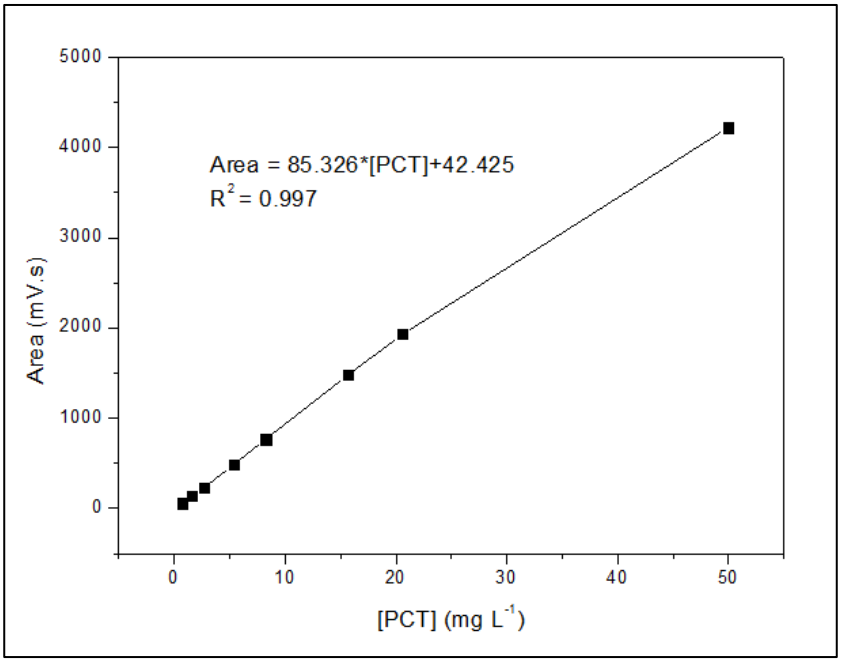

Source: own authorship

The preliminary tests using a mercury vapor lamp of 125W of power and radiation measured around 11 mW cm^{-2}, was not carried out until the end. The reason was that after doing some experiments it was possible to observe that there was no significant degradation of PCT. The results obtained by preliminary tests are given in Table 14 and

Figure 22. In the best experiment (E4) only 4% of paracetamol was degraded.

Table 14 - Results obtained in preliminary tests.

Run	Catalyst	pH	[cat] - (mg L^{-1})	C_t/C_0 last point	Paracetamol degradation (%)
E1	CFNb	3	300	1.06	0
E2	$CFNb_{600}$	3	300	1.01	0
E3	CFNb	9	300	1.00	0
E4	$CFNb_{600}$	9	300	0.96	4
E5	CFNb	6	100	0.99	1
E10	$CFNb_{300}$	9	100	0.99	1

Source: own authorship

Figure 22 - Graphical representation of the results obtained in the preliminary tests.

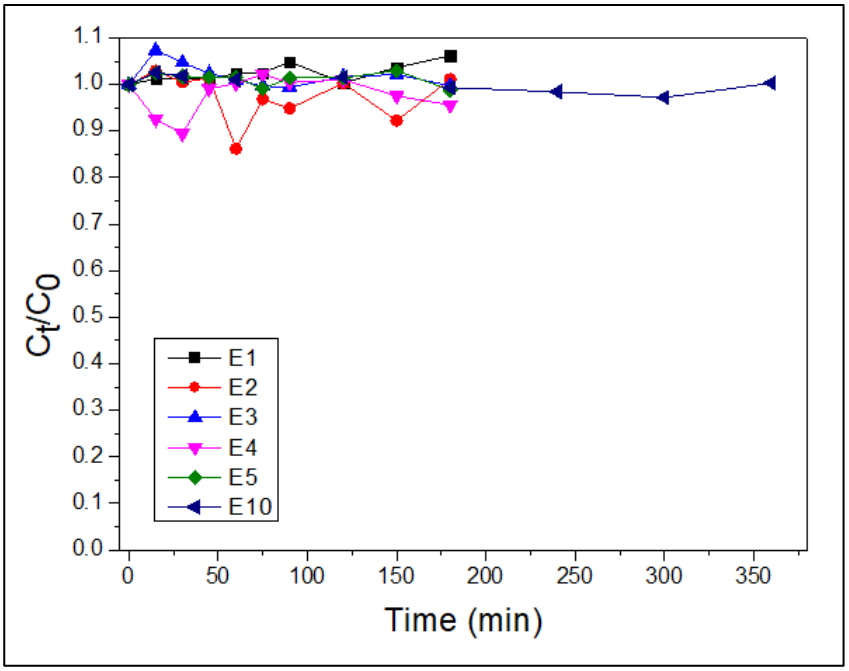

Source: own authorship

Given the result of the preliminary tests, it was thought to perform the catalytic process with some additive, in order to optimize the results. Thus, it was chosen to use formic acid (FONTANA *et al.*, 2018b), which was added to the procedure with the following variations: 0.01 mol L^{-1} without further adjustment of pH (pH approximately 2); and 0.01 mol L^{-1} with pH adjustment to 9 using NaOH. In addition to this change, another mercury vapor lamp was tested, with 250 W of power and measured radiation greater than 28 mW cm^{-2}. The variation in catalyst concentration remained between 100 and 300 mg L^{-1}, because as the catalyst is dark (tends to black), adding too much catalyst would darken the solution, impairing the radiation effect and decreasing the efficiency of the photocatalytic process.

All tests were performed with the CFNb catalyst, as it is the simplest to synthesize synthesize (there is no need for step 2), to be subsequently carried out with other catalysts at the optimum condition found with CFNb for the photocatalytic process under study. The results obtained in the tests of the design of experiments (DOE) are given in

Table 15 and Figure 23. It is possible to conclude that they are superior to the preliminary tests, reaching up to 59% of paracetamol degradation (experiment 4B).

Table 15 - Results obtained in the DOE.

Run	pH	Lamp power (W)	[cat] (mg L^{-1})	C_t/C_0 last point	Paracetamol degradation (%)
1A	2.45	125	301	0.85	15
2A	9.21	125	310	0.95	5
3A	2.16	125	102	0.93	7
4A	9.35	125	102	0.98	2
1B	2.61	250	302	0.52	48
2B	9.24	250	303	0.82	18
3B	2.12	250	100	0.41	59
4B	9.34	250	104	0.90	10

Source: own authorship

Figure 23 - Graphical representation of the results obtained in the DOE for paracetamol degradation

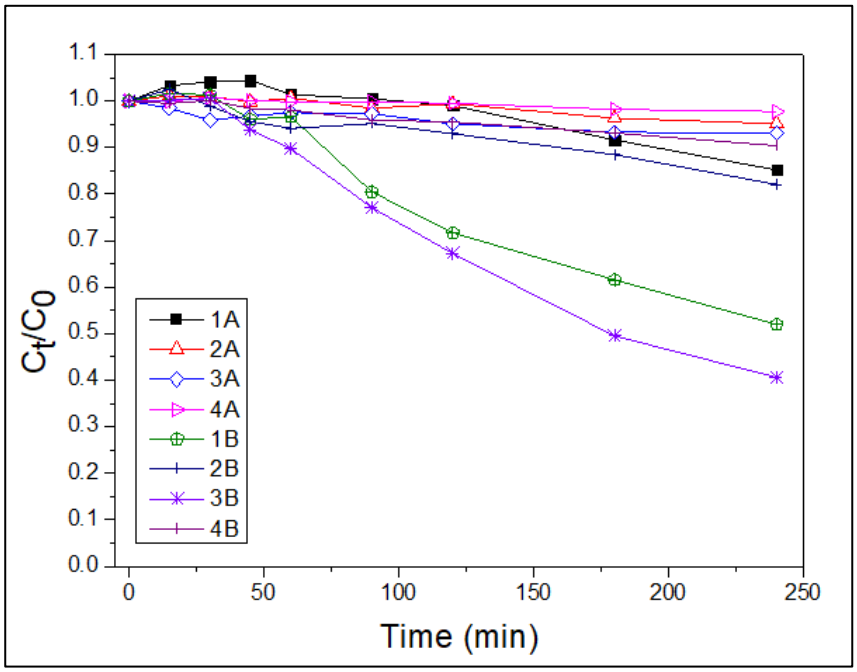

Source: own authorship

Formic acid is an additive widely used in photocatalytic processes, due to the characteristics of the formic acid molecule which, due to its reduced size, facilitates the contact on the surface of the catalyst, promoting its direct oxidation and enabling

greater degradation of PCT. In addition, the oxidation products of this additive are CO_2 and H_2O, which do not cause damage to the environment (FONTANA *et al*., 2018b). The inclusion of this additive was then positive to the process. Another factor that influenced better results was the use of a lamp with greater incident radiation, 2.5 times greater radiation, with double power.

To assess the influence of the 3 factors with two levels of variation, the DOE performed for 2^3, resulted in the 8 experiments listed in

Table 15. A statistical analysis of variance (ANOVA) allows to observe that in fact the DOE was not significant (p> 0.05). Table 16 contains the following parameters:

- sum of squares (SS);
- degrees of freedom (df);
- mean squares (MS), which is calculated by dividing a SS value by the corresponding df;
- ratio F (F), which is calculated by dividing the MS value by another MS value. For bidirectional ANOVA without repeated measures the denominator's MS value is always MS residual. For DOE the MS residual was 0.0057;
- p values (p), which must be less than 0.05 for the assessed factor to have significance in the DOE.

Table 16 - Analysis of variance for the DOE.

Factor	SS	df	MS	F	p
(1) pH	0.110	1	0.110	19.086	0.143
(2) Lamp power (W)	0.145	1	0.145	25.203	0.125
(3) [cat] (mg L^{-1})	0.001	1	0.001	0.205	0.729
1 by 2	0.052	1	0.052	9.124	0.203
1 by 3	0.001	1	0.001	0.203	0.730
2 by 3	0.002	1	0.002	0.292	0.685
Error	0.006	1	0.006		
Total SS	0.315	7			

Source: own authorship

Complementing this evaluation with the Pareto graph

Figure 24), the combination of factors is also not statistically significant for this DOE (p> 0.05 for all factors alone and in combination). When comparing in a graph the predicted values for DOE and the values observed experimentally (Figure 25), the experimental points, although close, do not belong to the line of predicted points, therefore DOE is not considered predictive.

Figure 24 - Pareto graph for the DOE.

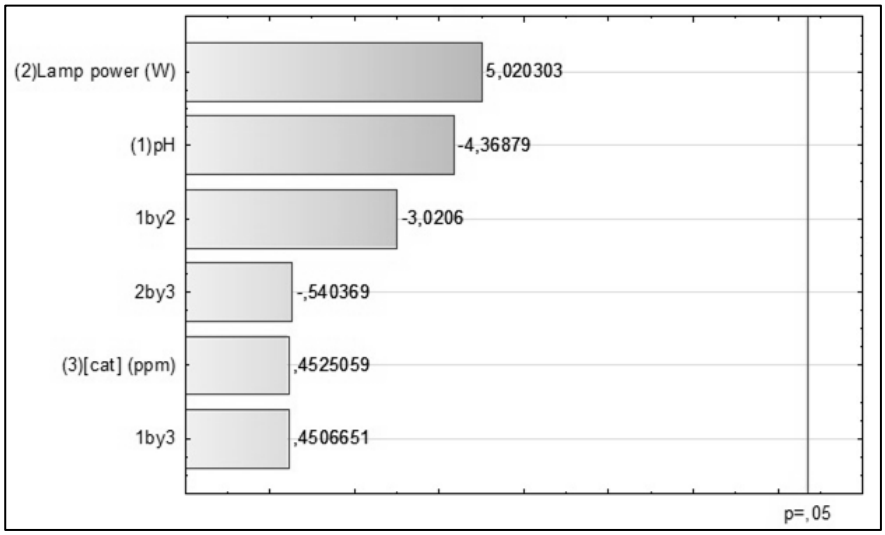

Source: own authorship

Figure 25 - Observed vs predicted values for the DOE.

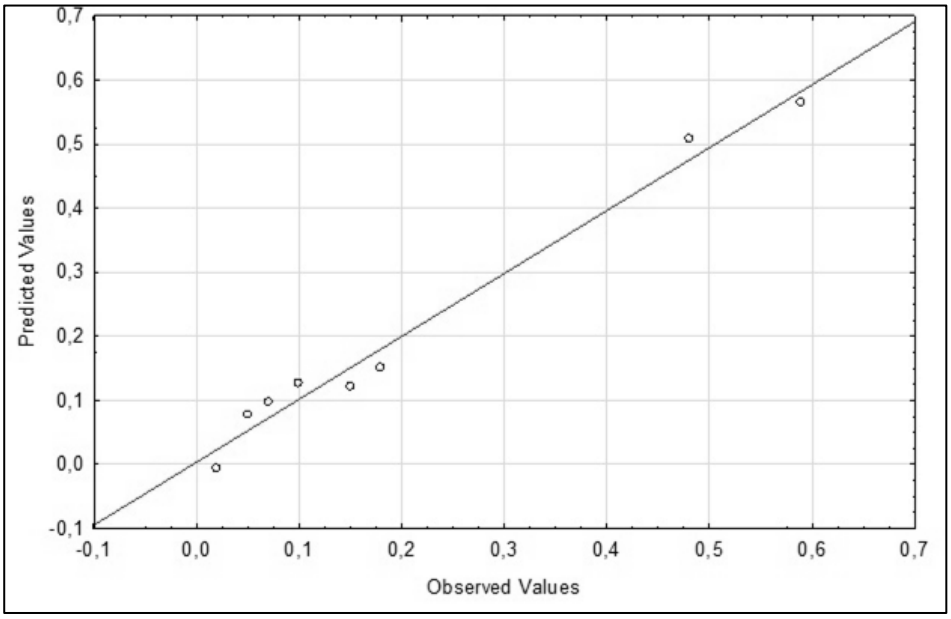

Source: own authorship

The response fitted surface in 3 and 2 dimensions are illustrated in Figure 26 (A) and (B), respectively. The adjusted equation is shown below Figure (A) with R^2 equal to 0.982. To define the surface, the lamp power factor was fixed at 250 W and the pH and [cat] parameters were varied. Even though R^2 is not so close to 1 and the factors were not statistically significant for DOE, it is possible to observe that better results can be obtained for pH closer to 1 and [cat] less than 200 mg L^{-1}.

Figure 26 - Response fitted surface (A) in 3D and (B) in 2D.

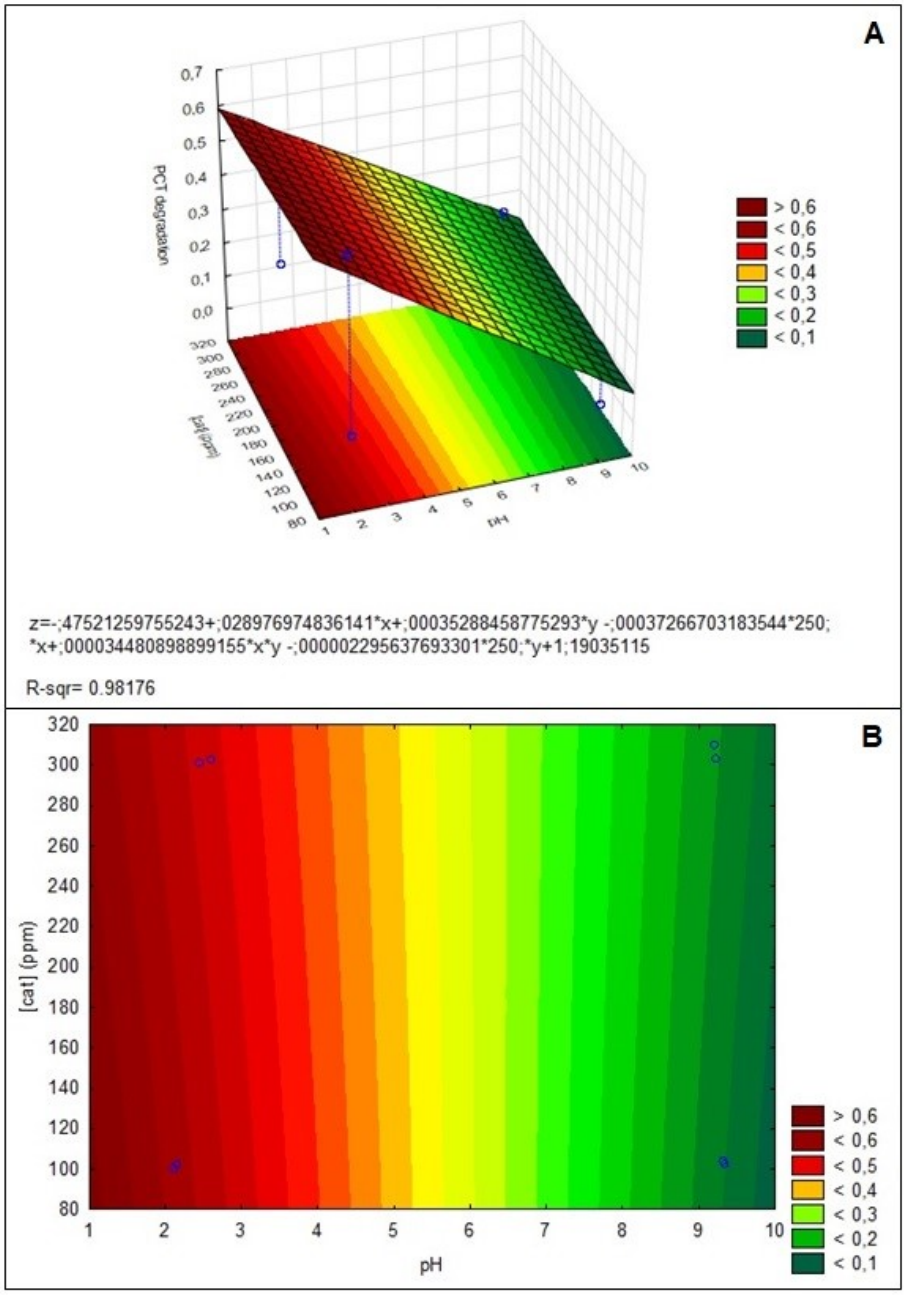

Source: own authorship

In order to evaluate the photocatalytic degradation of PCT, considering formic acid as an additive, at neutral pH and also at a very acid pH (around 1, which as shown by DOE would present better results), experiments 5B and 6B, respectively, were carried out. The pH was adjusted with the additive itself and with NaOH solution. The first experiment had a low PCT degradation, only 5%, while the second showed an average of 89% PCT degradation.

Among all the photocatalytic tests carried out, the best was obtained in run 6B. So, further reaction runs were performed for the same conditions of lamp power

(radiation), pH and catalyst concentration used in this test, however some changes were done to assess other factors that could influence degradation, such as:

- catalyst reuse, experiments 6B r1, 6B r2 and 6B r3, in which the catalyst CFNb was used after use in 6B, 6B r1 and 6B r2, respectively;
- adsorption test carried out without influence of radiation, to evaluate the adsorption capacity of the catalyst, experiment 6B adsorption;
- photolysis test performed without a catalyst, to assess degradation by radiation alone, 6B photolysis;
- long duration test performed for a longer time (24h instead of 4h), to assess whether there would be greater degradation over time or would have the state of equilibrium in 240 minutes of reaction, experiment 6B 24h;
- solar test made under solar radiation, experiment 6B solar.

The conditions and results are summarized in Table 17. The graph in Figure 27 allows to evaluate the degradation of PCT over the reaction time. The long reaction time (6B 24h) was represented separately with 6B for better observation, Figure 28.

Table 17 - Summary of reaction conditions and results obtained for catalyst CFNb.

Run	catalyst	pH	Lamp power	[cat] (mg L^{-1})	Ct/C0 last point	Paracetamol degradation (%)
5B	CFNb	7.97	250W	101	0.95	5
6B	CFNb	1.21	250W	102	0.11	89
6B r1	6B	1.56	250W	100	0.82	18
6B r2	6B r1	1.14	250W	102	0.79	21
6B r3	6B r2	1.42	250W	104	0.76	24
6B adsorption	CFNb	1.57	250W	102	1.03	0
6B photolysis	-	1.73	250W	0	0.77	23
6B 24h	CFNb	1.62	250W	103	0.30	70
6B solar	CFNb	1.69	250W	100	1.03	0

Source: own authorship

Figure 27 - Degradation of PCT at various conditions over time.

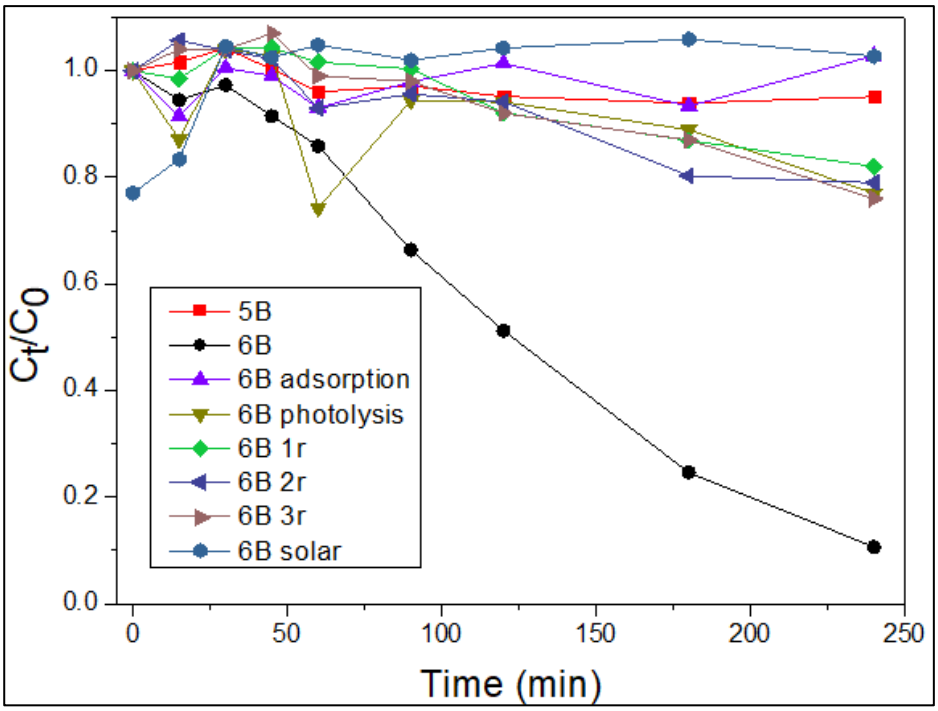

Source: own authorship

5.3.1 Solar degradation

The test under solar radiation was carried out with the climatic variations highly influencing this test, since there is no way to control it. During the 4 hours of experiment the radiation varied from 14 mW/m² at the beginning to 4 mW/m² at the end of the experiment, due to the presence of many clouds covering the sun. However, even the highest radiation during the experiment still represents half of that emitted by the 250 W mercury vapor lamp. Due to this reason the removal result obtained was practically insignificant.

5.3.2 Reuse

The reuse experiments were performed as follows: the catalyst used for experiment 6B was recovered at the end of 4 hours of reaction, centrifuged at 4000 rpm for 5 minutes (80-2B centrifuge, CENTRIBIO), washed with distilled water, dried in oven at 80 °C for approximately 6 hours and, finally, used for reaction 6B r1. The same procedure was performed with the catalyst after reaction 6B r1 to be applied to reaction 6B r2 and successively after reaction 6B r2 to use in reaction 6B r3.

The degradation of PCT upon reuse of the catalysts was lower than the degradation observed in run 6B (Table 17 and Figure 27), however, interestingly, among the reuses it was greater for the most reused catalyst. A complementary iron leaching test was carried out for the supernatants at the end of the 6B and 6B r3 reaction runs (on an A Analyst 700 atomic absorption equipment, Perkin Elmer). As result, 0.790 mg/L and 0.953 mg/L of iron were obtained in the reactions solutions 6B and 6B r3, which may represent that the amount of iron leached during the reuse reactions has influenced the composition of the catalyst and consequently the percentage of degradation of PCT.

5.3.3 Long time reaction

The long time reaction was carried out at practically the same conditions as considered in run 6B, but with a reaction time of 24 hours instead of 4 h, Figure 28. The pH factor was slightly higher for reaction 6B 24h, in that way the lower result may

have been influenced by this higher pH. As the same logic can be applied from experiment 3B to 6B, whose pH difference (in this case decreasing) improved the result.

Figure 28 - Comparison of reactions 6B and 6B 24h over time.

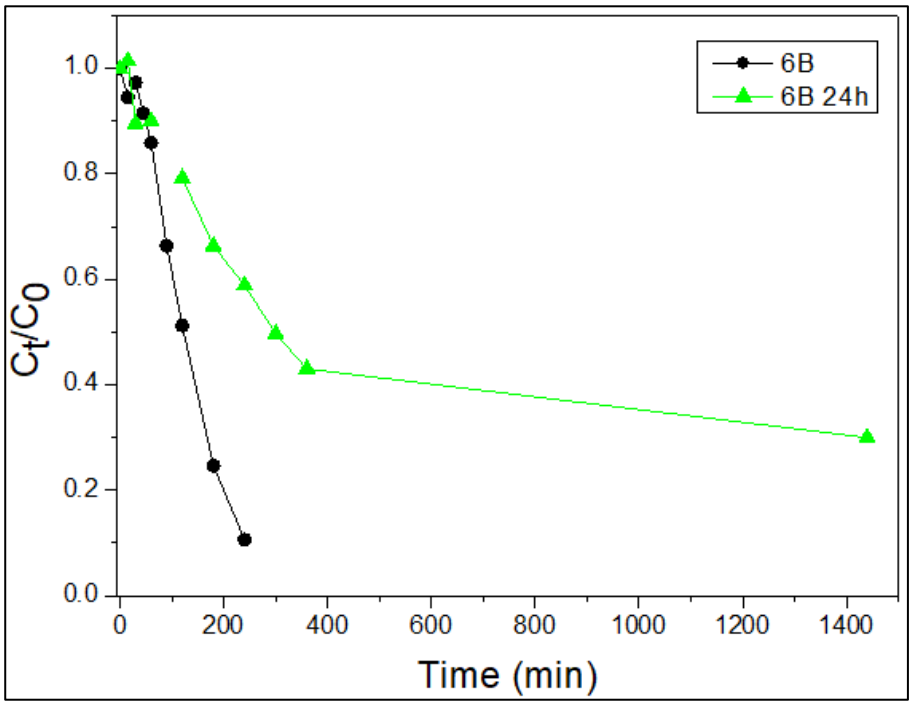

Source: own authorship

Among the various factors evaluated it can be noted that the conditions of experiment 6B, for the CFNb catalyst, were still the best for the degradation of PCT (89%). In view of this scenario, the other catalysts synthesized and characterized in this work were submitted under these conditions, as well as Nb_2O_5 alone without calcination (6B Nb) and cobalt ferrite alone, synthesized with tangerine peel extract (CFTE). The summary of the conditions and results are given in Table 18 and Figure 29.

Table 18 - Summary of reaction conditions and results obtained for several catalysts.

Run	catalyst	pH	Lamp power	[cat] (mg L^{-1})	C_t/C_0 last point	Paracetamol degradation (%)
6B100	$CFNb_{100}$	1.10	250W	101	0.02	98
6B200	$CFNb_{200}$	1.62	250W	102	0.43	57
6B300	$CFNb_{300}$	1.59	250W	101	0.58	42
6B400	$CFNb_{400}$	1.83	250W	101	0.62	38
6B500	$CFNb_{500}$	1.03	250W	103	0.01	99
6B600	$CFNb_{600}$	1.10	250W	102	0.04	96
6BCA	CFACNb	1.60	250W	102	0.52	48
6BNb	Nb_2O_5	1.73	250W	101	0.66	34
6BCF	CFTE	1.55	250W	104	0.29	71

Source: own authorship

Figure 29 - Degradation of PCT obtained with the various catalysts over time.

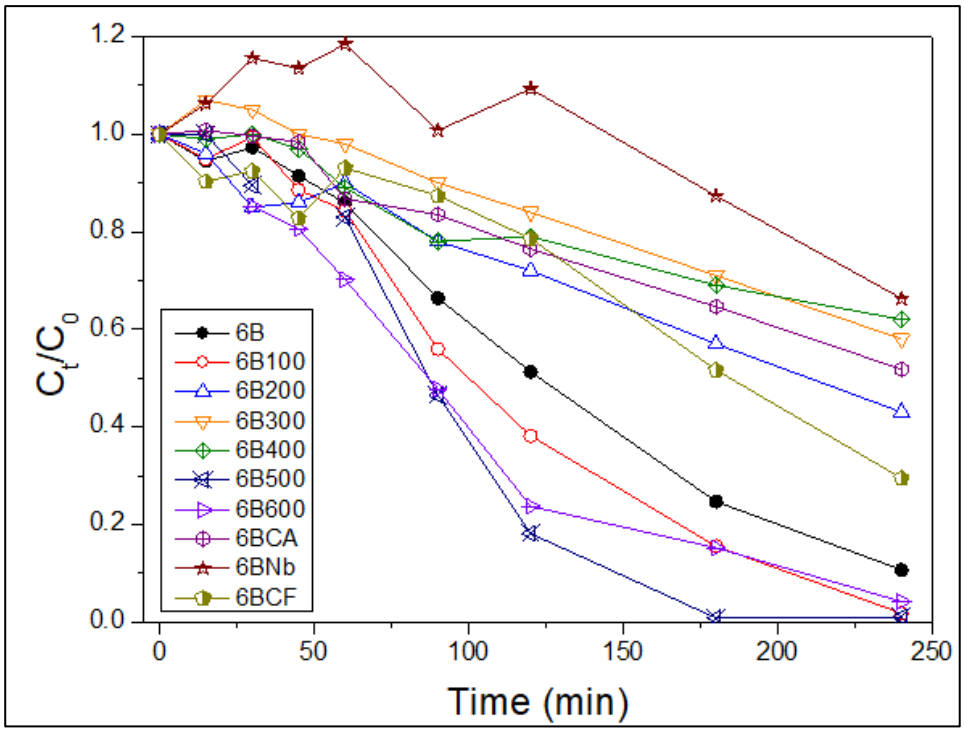

Source: own authorship

The catalysts $CFNb_{100}$, $CFNb_{500}$ and $CFNb_{600}$ demonstrated the best results for PCT degradation, 98, 99 and 96%, respectively. It is curious that the thermal treatment of niobium (step 2) did not seem to have as much influence on the structure and performance of the catalysts, as the Nb_2O_5 calcined at 100 °C showed similar results to those calcined at 500 and 600 °C, this possibly occurred due to calcination at 600 °C in step 3 (G-H). As the materials were evaluated in the experiments of photocatalysis and by photoacoustic characterization showed practically equal band-gap energies, it would be possible that they presented similar results among all during photocatalysis.

It is possible that the performance of the $CFNb_{100}$ catalyst is related to the larger S_{BET} of Nb_2O_5 and the smaller size of the final catalyst (178 m²/g and 22.78 nm, respectively). The larger surface allows greater contact with cobalt ferrite in step 3, which consequently would form smaller particles, which in turn have a lower tendency for agglomerations. In addition, $CFNb_{100}$ is the catalyst that has a higher proportion of oxygen in relation to the other elements, and oxygen is a fundamental element in photocatalysis.

The adsorption behavior of a defect-free surface is quite different from the real surface in which the presence of defects leads to greater photocatalytic activity. The defect-free surface is made up of columns of oxygen atoms (over the surface layer) bridged with the other atoms. Two types of defect sites can be produced by removing an oxygen atom from the bridge or an oxygen atom from the reticulum. Defects are bridge oxygen vacancy sites, oxygen vacancy sites in the reticulum and double oxygen bridge of the vacancy sites. Oxygen vacancies provide oxidation-reduction properties in addition to favoring adsorption processes on the catalyst surface. Adsorption is important to understand surface reactivity of the catalyst (ZIOLLI; JARDIM, 1998).

As for the $CFNb_{500}$ and $CFNb_{600}$ catalysts the characteristics are very similar, however the S_{BET} of the Nb_{500} is greater, 69 m²/g against 31 m²/g, so that the crystallite size of the $CFNb_{500}$ is slightly smaller than that of $CFNb_{600}$ (27.36 nm against 28.31 nm). The oxygen content is slightly higher for $CFNb_{500}$ than $CFNb_{600}$.

The Nb_2O_5 alone presented the worst result for experiments with different catalysts (34%) and CFTE presented an intermediate result (71%), which shows that the combination of the components of cobalt ferrite with niobium pentoxide is interesting for the photocatalysis process.

6 CONCLUSIONS

From the results obtained it is concluded that was successfully achieved the objective of creating a methodology via green synthesis, using extract from tangerine peel to obtain nanocatalysts composed of cobalt ferrite and niobium pentoxide. The methodology created, as well as the combination of elements considered, was worthy to patent attempt for the method and product obtained. Among several advantages of the synthesis, it can be highlighted the reuse of biomass residues, the low cost to obtain the material and the value added to a component richly disposed in the Brazilian territory (niobium).

With respect to the catalysts obtained, differentiated in the synthesis by the calcination temperature considered in step 2, it was noted by the characterizations that there are not major differences between them, but peculiarities that may make a difference depending on the desired conditions and applications.

The catalytic materials were active in the studied photocatalytic reaction of paracetamol degradation. Several experiments allowed to find the optimum operating conditions using formic acid 85% to adjust pH to 1, catalyst concentration of 100 mg L^{-1} and mercury vapor lamp power of 250 W. Under these conditions, for the catalysts $CFNb_{100}$, $CFNb_{500}$ and $CFNb_{600}$, PCT degradations of 98, 99 and 96% were obtained, fulfilling the objective of finding a photocatalysis conditions that would degrade the emerging pollutant paracetamol.

7 FUTURE RESEARCH

As an improvement of this work, there will be repetition of some photocatalytic experiments to verify the repeatability of the results and other conditions may be studied, in addition to performing the study of degradation kinetics. As well as the application of the catalysts in other catalytic processes, such as CWPO (catalytic wet peroxide oxidation) and to study the degradation of other pollutants such as different emerging pollutants, dyes and heavy metals.

To take advantage of the methodology created to obtain the materials developed in this work, variations of parameters will be explored, such as using peels from other fruits and/or organic industrial wastes. In addition, trying to obtain other magnetic materials supported on niobium pentoxide (like as magnetite). Furthermore, as seen that the heat treatment of Nb_2O_5 was not significant in step 2, perhaps replace it with a calcination between 800 and 900 °C to verify the influence of the monoclinic phase of niobium pentoxide, and if there is still no significant influence, to conduct more research studies using only Nb_2O_5 without calcination, eliminating step 2.

REFERENCES

3P-INSTRUMENT. **BET surface area**. Available in: <https://www.3p-instruments.com/measurement-methods/bet-surface-area/#measurement-methods-bet-surface-area>. Accessed: Dec. 16, 2020.

ABDEL-WAHAB, A.-M. *et al*. Photocatalytic degradation of paracetamol over magnetic flower-like TiO_2/Fe_2O_3 core-shell nanostructures. **Journal of Photochemistry and Photobiology A: Chemistry**, v. 347, p. 186-198, Oct. 2017.

AFINKO. **MEV: Entenda o que faz a Microscopia Eletrônica de Varredura?** Available in: <https://afinkopolimeros.com.br/o-que-e-microscopia-eletronica-mev/>. Accessed: Feb. 23, 2021.

AL-KAF, A. G. *et al*. Occurrence of paracetamol in aquatic environments and transformation by microorganisms: a review. **Chronicles of Pharmaceutical Science**, v. 1, n. 6, p. 341-355, 2017.

ALI, S.; MOHD ZABIDI, N. A.; SUBBARAO, D. Effect of niobium promoters on iron-based catalysts for Fischer-Tropsch reaction. **Journal of Fuel Chemistry and Technology**, v. 40, n. 1, p. 48-53, Jan. 2012.

AMETA, R.; AMETA, S. C. **Nanoparticles and Catalysis**. 1. ed. [s.l.] Wiley, 2007.

AMIRI, M. *et al*. Caffeine: A novel green precursor for synthesis of magnetic CoFe2O4 nanoparticles and pH-sensitive magnetic alginate beads for drug delivery. **Materials Science and Engineering: C**, v. 76, p. 1085-1093, Jul. 2017a.

AMIRI, M. *et al*. Removal of malachite green (a toxic dye) from water by cobalt ferrite silica magnetic nanocomposite: Herbal and green sol-gel autocombustion synthesis. **International Journal of Hydrogen Energy**, v. 42, n. 39, p. 24846-24860, Sep. 2017b.

AMJAD, U. *et al*. MgO and Nb_2O_5 oxides used as supports for Ru-based catalysts for the methane steam reforming reaction. **Catalysis Today**, v. 257, n. P1, p. 122-130, Nov. 2015.

ANASTAS, P.; WARNER, J. **12 Principles of Green Chemistry**. Available in: <https://www.acs.org/content/acs/en/greenchemistry/principles/12-principles-of-green-chemistry.html>. Accessed: Feb. 23, 2021

AUGUSTO, T. D. M. *et al*. Iron ore tailings as catalysts for oxidation of the drug paracetamol and dyes by heterogeneous Fenton. **Journal of Environmental Chemical Engineering**, v. 6, n. 5, p. 6545-6553, Oct. 2018.

BAVASSO, I.; POGGI, C.; PETRUCCI, E. Enhanced degradation of paracetamol by combining UV with electrogenerated hydrogen peroxide and ozone. **Journal of Water Process Engineering**, v. 34, p. 101102, Apr. 2020.

BHADURI, S.; MUKESH, D. **Homogeneous catalysis:** mechanisms and Industrial Applications. 1. ed. [s.l.] Wiley Interscience, 2000.

BHAGWAT, V. R. *et al*. Sol-gel auto combustion synthesis and characterizations of cobalt ferrite nanoparticles: Different fuels approach. **Materials Science and Engineering: B**, v. 248, n. 2, p. 114388, Sep. 2019.

Bula do Paracetamol. Available in: <https://consultaremedios.com.br/paracetamol/bula>. Accessed: Jan. 8, 2021.

CALAS-BLANCHARD, C. *et al*. Biosensor-based real-time monitoring of paracetamol photocatalytic degradation. **Chemosphere**, v. 131, p. 124-129, Jul. 2015.

CARRASCO-DÍAZ, M. R. *et al*. On the textural and crystalline properties of Fe-carbon xerogels. Application as Fenton-like catalysts in the oxidation of paracetamol by H_2O_2. **Microporous and Mesoporous Materials**, v. 237, p. 282-293, Jan. 2017.

CARVALHO, F. E. *et al*. Structural and complex electromagnetic properties of cobalt ferrite ($CoFe_2O_4$) with an addition of niobium pentoxide. **Ceramics International**, v. 44, n. 1, p. 915-921, Jan. 2018.

CASTRO, D. C. *et al*. Synthesis and Characterization of Mesoporous Nb_2O_5 and Its Application for Photocatalytic Degradation of the Herbicide Methylviologen. **Journal of the Brazilian Chemical Society**, v. 27, n. 2, p. 303-313, 2016.

CHAVARRIAGA, E. A. *et al*. Gel combustion synthesis and magnetic properties of $CoFe_2O_4$, $ZnFe_2O_4$, and $MgFe_2O_4$ using 6-aminohexanoic acid as a new fuel. **Journal of Magnetism and Magnetic Materials**, v. 497, p. 166054, Mar. 2020.

DE ASSUMPÇÃO PEREIRA-DA-SILVA, M.; FERRI, F. A. Scanning Electron Microscopy. In: **Nanocharacterization Techniques**. [s.l.] Elsevier, 2017. 272p. 1-35.

DUPONT, J. A catálise no Brasil nos últimos 25 anos: uma história de sucesso. **Química Nova**, v. 25, n. 1, p. 12-13, 2002.

DURMUŞ, A.; ÇOLAK, H.; KARAKÖSE, E. Production and examination of ZnO thin film for first time using green synthesized method from aqueous Citrus reticulata peel extract. **Journal of Alloys and Compounds**, v. 809, p. 151813, Nov. 2019.

ERTL, G. *et al*. (ed.). **Handbook of Heterogeneous Catalysis**. Weinheim, Germany: Wiley-VCH Verlag GmbH & Co. KGaA, 2008. v. 1

FALK, G. *et al*. Microwave-assisted synthesis of Nb_2O_5 for photocatalytic application of nanopowders and thin films. **Journal of Materials Research**, v. 32, n. 17, p. 3271-3278, 27 Sep. 2017.

FARAJI, M.; YAMINI, Y.; REZAEE, M. Magnetic nanoparticles: synthesis, stabilization, functionalization, characterization, and applications. **Journal of the Iranian Chemical Society**, v. 7, n. 1, p. 1-37, Mar. 2010.

FARMACOCINÉTICA Paracetamol. Available in: <https://www.bulas.med.br/p/detalhamento-das-bulas/1187419/farmacocinetica+paracetamol.htm>. Accessed: Nov.12, 2020

FIDELIS, M. *et al*. Experimental Design and Optimization of Triclosan and 2.8-Diclorodibenzeno-p-dioxina Degradation by the Fe/Nb_2O_5/UV System. **Catalysts**, v. 9, n. 4, p. 343, Apr. 8, 2019.

FIDELIS, M. Z. **Degradação de triclosan e 2,8-diclorodibenzeno-p- dioxina via sistema Fe/Nb_2O_5/UV**. 2019. Dissertação (Mestrado em Engenharia Química). Universidade Tecnológica Federal do Paraná - Ponta Grossa, 2019. Available in: <http://repositorio.utfpr.edu.br/jspui/handle/1/3987>.

FONTANA, K. B. *et al*. Comparision of photocatalysis and photolysis processes for arsenic oxidation in water. **Ecotoxicology and Environmental Safety**, v. 151, n. January, p. 127-131, Apr. 2018a.

FONTANA, K. B. *et al*. Barium removal by photocatalytic process: An alternative for water treatment. **Journal of Water Process Engineering**, v. 22, n. January, p. 163-171, Apr. 2018b.

GHOSH, M.; SWAIN, K. K.; VERMA, R. Interaction of niobium with iron-oxide colloids and the role of humic acid. **Journal of Environmental Radioactivity**, v. 178-179, p. 101-109, Nov. 2017.

GINGASU, D. *et al*. Green synthesis methods of $CoFe_2O_4$ and Ag-$CoFe_2O_4$ nanoparticles using Hibiscus extracts and their antimicrobial potential. **Journal of Nanomaterials**, 2016a.

GINGASU, D. *et al*. Synthesis of nanocrystalline cobalt ferrite through soft chemistry methods: A green chemistry approach using sesame seed extract. **Materials Chemistry and Physics**, v. 182, p. 219-230, 2016b.

GOMES, H. T. *et al*. The role of activated carbons functionalized with thiol and sulfonic acid groups in catalytic wet peroxide oxidation. **Applied Catalysis B: Environmental**, v. 106, n. 3-4, p. 390-397, Aug. 2011.

GREENWOOD, N. N.; EARNSHAW, A. **Chemistry of the Elements**. 2 nd ed. Oxford, UK: Butterworth-Heinemann, 1997.

GUARINO, M. E. *et al*. Avaliação da eficiência de catalisadores à base de cobre, ferro, níquel e cobalto , suportados em óxido de nióbio, na redução do óxido nítrico por monóxido de carbono. **Exatas Online**, v. 5, n. 1, p. 13-28, 2014.

HARSHINY, M.; ISWARYA, C. N.; MATHESWARAN, M. Biogenic synthesis of iron nanoparticles using Amaranthus dubius leaf extract as a reducing agent. **Powder Technology**, v. 286, p. 744-749, 2015.

HE, J. *et al*. Hydrothermal growth and optical properties of Nb_2O_5 nanorod arrays. **Journal of Materials Chemistry C**, v. 2, n. 38, p. 8185-8190, 2014.

HERRMANN, J. M. Heterogeneous photocatalysis: Fundamentals and applications to the removal of various types of aqueous pollutants. **Catalysis Today**, v. 53, n. 1, p. 115-129, Oct. 1999.

HINOJOSA GUERRA, M. M. *et al*. Oxidation mechanisms of amoxicillin and paracetamol in the photo-Fenton solar process. **Water Research**, v. 156, p. 232-240, Jun. 2019.

HUANG, L. *et al*. Green synthesis of iron nanoparticles by various tea extracts: Comparative study of the reactivity. **Spectrochimica Acta Part A: Molecular and Biomolecular Spectroscopy**, v. 130, p. 295-301, Sep. 2014.

HUANG, M. *et al*. Magnetic iron nanoparticles prepared by solution combustion synthesis and hydrogen reduction. **Chemical Physics Letters**, v. 657, p. 33-38, Jul. 2016.

IANOȘ, R. Highly sinterable cobalt ferrite particles prepared by a modified solution combustion synthesis. **Materials Letters**, v. 135, p. 24-26, Nov. 2014.

IBGE - PRODUÇÃO AGRÍCOLA MUNICIPAL. **Produção de lavouras permanentes: Tangerina**. Available in: <https://sidra.ibge.gov.br/tabela/1613#resultado>. Accessed: Out. 15, 2020.

ITUEN, E. *et al*. Green synthesis of Citrus reticulata peels extract silver nanoparticles and characterization of structural, biocide and anticorrosion properties. **Journal of Molecular Structure**, v. 1207, p. 127819, May 2020.

JAGANNATHAN, M.; GRIESER, F.; ASHOKKUMAR, M. Sonophotocatalytic degradation of paracetamol using TiO_2 and Fe^{3+}. **Separation and Purification Technology**, v. 103, p. 114-118, Jan. 2013.

JALLOULI, N. *et al*. Photocatalytic degradation of paracetamol on TiO_2 nanoparticles and TiO_2/cellulosic fiber under UV and sunlight irradiation. **Arabian Journal of Chemistry**, v. 10, p. S3640-S3645, May 2017.

JESSICA R P OLIVEIRA. **Development and functionalization of magnetic nanocomposites for cancer treatment**. 2017. Thesis report (Master Degree in Chemical Engineering).Instituto Politécnico de Bragança, 2017. Available in: <https://bibliotecadigital.ipb.pt/bitstream/10198/14597/1/Jessica do Rocio de Paula de Oliveira.pdf>.

KEFENI, K. K.; MAMBA, B. B.; MSAGATI, T. A. M. Magnetite and cobalt ferrite nanoparticles used as seeds for acid mine drainage treatment. **Journal of Hazardous Materials**, v. 333, p. 308-318, Jul. 2017.

KHARISSOVA, O. V. *et al*. Greener synthesis of chemical compounds and materials. **Royal Society Open Science**, v. 6, n. 11, p. 191378, Nov. 2019.

KHASAWNEH, O. F. S.; PALANIANDY, P.; TENG, L. P. Large-scale study for the photocatalytic degradation of paracetamol using Fe_2O_3/TiO_2 nanocomposite catalyst and CPC reactor under natural sunlight radiations. **MethodsX**, v. 6, p. 2735-2743, 2019.

KÖNIG, B. **Chemical Photocatalysis**. Berlin, Germany: DE GRUYTER, 2013.

LI, G.-L. *et al*. Tangerine peel-derived carbon supported manganese oxides catalyst for oxygen reduction reaction. **Applied Surface Science**, v. 450, p. 251-259, Aug. 2018.

LI, S. *et al*. Comparison of amorphous, pseudohexagonal and orthorhombic Nb_2O_5 for high-rate lithium ion insertion. **CrystEngComm**, v. 18, n. 14, p. 2532-2540, 2016.

LIAO, J. *et al*. Controlling the morphology, size and phase of Nb_2O_5 crystals for high electrochemical performance. **Chinese Chemical Letters**, v. 29, n. 12, p. 1785-1790, Dec. 2018.

LIU, M.; XUE, D. Large-scale fabrication of $H_2(H_2O)Nb_2O_6$ and Nb_2O_5 hollow microspheres. **Materials Research Bulletin**, v. 45, n. 3, p. 333-338, Mar. 2010.

LONG, N. V. *et al*. Synthesis and magnetism of hierarchical iron oxide particles. **Materials and Design**, v. 86, p. 797-808, 2015.

MACHADO, S. *et al*. Characterization of green zero-valent iron nanoparticles produced with tree leaf extracts. **Science of The Total Environment**, v. 533, p. 76-81, Nov. 2015.

MAKAROV, V. V. *et al*. Biosynthesis of stable iron oxide nanoparticles in aqueous extracts of hordeum vulgare and rumex acetosa plants. **Langmuir**, v. 30, n. 20, p. 5982-5988, May 2014.

MARTÍNEZ-CABANAS, M. *et al*. Green synthesis of iron oxide nanoparticles. Development of magnetic hybrid materials for efficient As(V) removal. **Chemical Engineering Journal**, v. 301, p. 83-91, 2016.

MASUDI, A. *et al*. Equidistant crystal distortion arrangement of copper doped magnetite for paracetamol degradation and optimization with response surface methodology (RSM). **Materials Chemistry and Physics**, v. 250, n. Nov. 2019, p. 122995

MITRA, D. *et al*. Emerging pharmaceutical and organic contaminants removal using carbonaceous waste from oil refineries. **Chemosphere**, v. 271, p. 129542, May 2021.

MOCTEZUMA, E. *et al*. Photocatalytic degradation of paracetamol: intermediates and total reaction mechanism. **Journal of Hazardous Materials**, v. 243, p. 130-138, Dec. 2012.

MOLINARI, A. *et al*. Degradation of emerging concern contaminants in water by heterogeneous photocatalysis with $Na_4W_{10}O_{32}$. **Applied Catalysis B: Environmental**, v. 203, p. 9-17, Apr. 2017.

MORAWA EBLAGON, K. *et al*. Impact of thermal treatment of Nb_2O_5 on its performance in glucose dehydration to 5-hydroxymethylfurfural in water. **Nanomaterials**, v. 10, n. 9, p. 1685, Aug. 2020.

NAPOLEÃO, D. C. *et al*. Degradação do contaminante emergente paracetamol empregando processos oxidativos avançados. **Revista Eletrônica em Gestão Educação e Tecnologia Ambiental**, v. 19, n. 3, p. 725-734, 2015.

NAVA, O. J. *et al*. Fruit peel extract mediated green synthesis of Zinc Oxide nanoparticles. **Journal of Molecular Structure**, 2017.

NÚÑEZ, O. *et al*. A closer look inside TiO_2(P25) photocatalytic CO_2/HCO_3^- reduction with water. Methane rate and selectivity enhancements. **Chemical Engineering Journal**, v. 409, n. Dec. 2020, p. 128141.

OLIVEIRA, J. R. P. *et al*. Carbon-based magnetic nanocarrier for controlled drug release: a green synthesis approach. **Journal of Carbon Research**, v. 5, 2018.

PANALYTICAL, M. **X-ray analysis**. Available in: <https://www.malvernpanalytical.com/br/products/technology/xray-analysis>. Accessed: Dec.16, 2020.

PAUMO, H. K. *et al*. TiO_2 assisted photocatalysts for degradation of emerging organic pollutants in water and wastewater. **Journal of Molecular Liquids**, p.115458, Feb. 2021.

PESQUEIRA, J. F. J. R.; PEREIRA, M. F. R.; SILVA, A. M. T. Environmental impact assessment of advanced urban wastewater treatment technologies for the removal of priority substances and contaminants of emerging concern: A review. **Journal of Cleaner Production**, v. 261, p. 121078, Jul. 2020.

PESSOA, C. **No final das contas, o que é nióbio?** Available in: <https://www.tecmundo.com.br/ciencia/132827-final-contas-niobio.htm>. Accessed: Apr. 21, 2020.

PETRE, A. . *et al*. Characterization and reactivity of group III oxides supported on niobium oxide. **Catalysis Today**, v. 78, p. 377-386, Feb. 2003.

POGHOSSIAN, A. A. Determination of the pHpzc of insulators surface from capacitance-voltage characteristics of MIS and EIS structures. **Sensors and Actuators B: Chemical**, v. 44, n. 1-3, p. 551-553, Oct. 1997.

PRASAD, C.; GANGADHARA, S.; VENKATESWARLU, P. Bio-inspired green synthesis of Fe_3O_4 magnetic nanoparticles using watermelon rinds and their catalytic activity. **Applied Nanoscience**, v. 6, n. 6, p. 797-802, 2016.

PURNAMA, B.; WIJAYANTA, A. T.; SUHARYANA. Effect of calcination temperature on structural and magnetic properties in cobalt ferrite nano particles. **Journal of King Saud University - Science**, v. 31, n. 4, p. 956-960, Oct. 2019.

RAD, L. R. *et al*. Simultaneous degradation of phenol and paracetamol during photo-Fenton process: Design and optimization. **Journal of the Taiwan Institute of Chemical Engineers**, v. 47, p. 190-196, Feb. 2015.

RAMCHANDRA KIRAN, R. *et al*. Structural, magnetic and magnetoelectric properties of Nb substituted Cobalt Ferrite. **Journal of Alloys and Compounds**, v. 610, p. 517-521, Oct. 2014.

RANI, B. J. *et al*. Ferrimagnetism in cobalt ferrite ($CoFe_2O_4$) nanoparticles. **Nano-Structures and Nano-Objects**, v. 14, p. 84-91, 2018.

RIBEIRO, R. S. *et al*. Hybrid magnetic graphitic nanocomposites towards catalytic wet peroxide oxidation of the liquid effluent from a mechanical biological treatment plant for municipal solid waste. **Applied Catalysis B: Environmental**, v. 219, p. 645-657, Dec. 2017.

RIBEIRO, R. S. *et al*. Enhanced performance of cobalt ferrite encapsulated in graphitic shell by means of AC magnetically activated catalytic wet peroxide oxidation of 4-nitrophenol. **Chemical Engineering Journal**, v. 376, p. 120012, Nov. 2019.

ROSS, J. R. H. **Heterogeneuos Catalysis: Fundamentals and Applications**. 1. ed. [s.l.] Elsevier, 2011.

RUEDA-MARQUEZ, J. J. *et al*. A critical review on application of photocatalysis for toxicity reduction of real wastewaters. **Journal of Cleaner Production**, v. 258, Jun. 2020.

RUEDA, D. *et al*. Low-cost tangerine peel waste mediated production of Titanium Dioxide Nanocrystals: Synthesis and characterization. **Environmental Nanotechnology, Monitoring & Management**, v. 13, p. 100285, May 2020.

RUTGER A. VAN SANTEN. **Theoretical Heterogeneous Catalysis**. Singapore, Singapore: World Scientific, 1991. v. 5

SAJJIA, M. *et al*. Development of cobalt ferrite powder preparation employing the sol-gel technique and its structural characterization. **Journal of Alloys and Compounds**, v. 506, n. 1, p. 400-406, Sep. 2010.

SALIHU, R. *et al*. Citric acid: A green cross-linker of biomaterials for biomedical applications. **European Polymer Journal**, v. 146, p. 110271, Mar. 2021.

SANTOS SILVA, A. *et al*. Wet peroxide oxidation of paracetamol using acid activated and fe/co-pillared clay catalysts prepared from natural clays. **Catalysts**, v. 9, n. 9, p. 705, Aug. 2019.

SEO, H.; KIM, K.; KIM, J.-H. Spherical Sb Core/Nb_2O_5-C double-shell structured composite as an anode material for li secondary batteries. **Energies**, v. 13, n. 8, p. 1999, 17 abr. 2020.

SHANMUGAVEL, T. *et al*. Single step synthesis and characterisation of nanocrystalline cobalt ferrite by auto-combustion method. **Materials Today: Proceedings**, v. 2, n. 4-5, p. 3605-3609, 2015.

SHI, Z. *et al*. Mesoporous superparamagnetic cobalt ferrite nanoclusters: Synthesis, characterization and application in drug delivery. **Journal of Magnetism and Magnetic Materials**, v. 498, p. 166222, Mar. 2020.

SHIMADZU. **ABC's of Photoacoustic Spectroscopy**. Available in: <https://www.shimadzu.com/an/service-support/technical-support/analysis-basics/ftirtalk/talk7.html>. Accessed: Dec. 16, 2020.

SILVA, A. S. **Treatment of wastewater containing pharmaceutical compounds by catalytic wet peroxide oxidation using clay-based materials as catalysts**. 2019. Thesis report (Master Degree in Chemical Engineering).Instituto Politécnico de Bragança, 2019. Available in: <https://bibliotecadigital.ipb.pt/handle/10198/19537>.

SILVA, M. K. *et al*. Evaluation of Nb_2O_5 and Ag/Nb_2O_5 in the photocatalytic degradation of dyes from textile industries. **Brazilian Journal of Chemical Engineering**, v. 19, n. 4, p. 359-363, Dec. 2002.

SLAMANI, S. *et al*. Initiation of Fenton process by plasma gliding arc discharge for the degradation of paracetamol in water. **Journal of Photochemistry and Photobiology A: Chemistry**, v. 359, p. 1-10, May 2018.

SNEHA SHAH, SUMITA DASGUPTA, MOUSUMI CHAKRABORTY, RAJI VADAKKEKARA, M. H. Green synthesis of iron nanoparticles using plant extracts. **International Jornal of Biological & Pharmaceutical Recearch**, v. 5, n. 6, p. 549-552, 2014.

SONU *et al*. Review on augmentation in photocatalytic activity of $CoFe_2O_4$ via heterojunction formation for photocatalysis of organic pollutants in water. **Journal of Saudi Chemical Society**, v. 23, n. 8, p. 1119-1136, Dec. 2019.

TAN, C. *et al*. Efficient degradation of paracetamol with nanoscaled magnetic $CoFe_2O_4$ and $MnFe_2O_4$ as a heterogeneous catalyst of peroxymonosulfate. **Separation and Purification Technology**, v. 175, p. 47-57, Mar. 2017.

THOMMES, M. *et al*. Physisorption of gases, with special reference to the evaluation of surface area and pore size distribution (IUPAC Technical Report). **Pure and Applied Chemistry**, v. 87, n. 9-10, p. 1051-1069, Oct. 2015.

UNITED STATES ENVIRONMENTAL PROTECTION AGENCY. **Basics of Green Chemistry**. Available in: <https://www.epa.gov/greenchemistry/basics-green-chemistry#:~:text=Definition of green chemistry,-Green chemistry is&text=Green chemistry%3A&text=Reduces the negative impacts of,to reduce their intrinsic hazards>. Accessed: Feb. 23, 2021.

USDA. **Citrus:World Markets and Trade**. Available in: <https://www.fas.usda.gov/data/citrus-world-markets-and-trade>. Accessed: Jan. 8, 2021.

VAIANO, V.; SACCO, O.; MATARANGOLO, M. Photocatalytic degradation of paracetamol under UV irradiation using TiO_2-graphite composites. **Catalysis Today**, v. 315, p. 230-236, Oct. 2018.

VALBONESI, P. *et al*. Contaminants of emerging concern in drinking water: Quality assessment by combining chemical and biological analysis. **Science of The Total Environment**, v. 758, p. 143624, Mar. 2021.

VARGAS-BERRONES, K. *et al*. Emerging pollutants (EPs) in Latin América: A critical review of under-studied EPs, case of study -Nonylphenol-. **Science of The Total Environment**, v. 726, p. 138493, Jul. 2020.

VENTURINI, J. *et al*. Sol-gel synthesis of substoichiometric cobalt ferrite ($CoFe_2O_4$) spinels: Influence of additives on their stoichiometry and magnetic properties. **Ceramics International**, v. 44, n. 11, p. 12381-12388, Aug. 2018.

WANG, L.; BIAN, Z. Photocatalytic degradation of paracetamol on Pd-BiVO4 under visible light irradiation. **Chemosphere**, v. 239, p. 124815, Jan. 2020.

WANG, T. *et al*. Green synthesized iron nanoparticles by green tea and eucalyptus leaves extracts used for removal of nitrate in aqueous solution. **Journal of Cleaner Production**, v. 83, p. 413-419, Nov. 2014.

WANG, Z.; FANG, C.; MALLAVARAPU, M. Characterization of iron-polyphenol complex nanoparticles synthesized by Sage (Salvia officinalis) leaves. **Environmental Technology & Innovation**, v. 4, p. 92-97, Oct. 2015.

WU, S.; ZHANG, L.; CHEN, J. Paracetamol in the environment and its degradation by microorganisms. **Applied Microbiology and Biotechnology**, v. 96, n. 4, p. 875-884, Nov. 2012.

WU, Y. *et al*. Heterogeneous Fenton-like oxidation of malachite green by iron-based nanoparticles synthesized by tea extract as a catalyst. **Separation and Purification Technology**, v. 154, p. 161-167, Nov. 2015.

XIANG, W. *et al*. Catalysts promoted with niobium oxide for air pollution abatement. **Catalysts**, v. 7, n. 5, p. 144, May 2017.

XU, D. *et al*. Cobalt-free niobium-doped barium ferrite as potential materials of dense ceramic membranes for oxygen separation. **Journal of Membrane Science**, v. 455, p. 75-82, Apr. 2014.

YADAV, D. *et al*. Environmental and health impacts of contaminants of emerging concerns: Recent treatment challenges and approaches. **Chemosphere**, v. 272, p. 129492, Jun. 2021.

YAKUBU, A. *et al*. Effect of temperature on structural, magnetic and dielectric properties of cobalt ferrite nanoparticles prepared via co-precipitation method. **Physical Science International Journal**, v. 8, n. 1, p. 1-8, Jan. 2015.

YANG, L.; YU, L. E.; RAY, M. B. Degradation of paracetamol in aqueous solutions by TiO_2 photocatalysis. **Water Research**, v. 42, p. 3480-3488, Jul. 2008.

YU, M. *et al*. Intimate coupling of photocatalysis and biodegradation for wastewater treatment: Mechanisms, recent advances and environmental applications. **Water Research**, v. 175, p. 115673, May 2020.

ZENG, G.-Y. *et al*. Fabrication of Nb_2O_5/C nanocomposites as a high performance anode for lithium ion battery. **Chinese Chemical Letters**, v. 28, n. 4, p. 755-758, Apr. 2017.

ZHANG, J. *et al*. **Photocatalysis: Fundamentals, Materials and Applications**. Singapore: Springer Singapore, 2018. v. 100

ZHU, D.; ZHOU, Q. Action and mechanism of semiconductor photocatalysis on degradation of organic pollutants in water treatment: A review. **Environmental Nanotechnology, Monitoring and Management**, v. 12, p. 100255, 2019.

ZIOLLI, R. L.; JARDIM, W. F. Mecanismo de fotodegradação de compostos orgânicos catalisada por TiO_2. **Química Nova**, v. 21, n. 3, p. 319-325, Jun. 1998.

ŻUR, J. *et al*. Organic micropollutants paracetamol and ibuprofen—toxicity, biodegradation, and genetic background of their utilization by bacteria. **Environmental Science and Pollution Research**, v. 25, n. 22, p. 21498-21524, Aug. 2018.

APPENDIX A - SEM/EDS characterization images of the catalysts CFNb, $CFNb_{100}$, $CFNb_{200}$, $CFNb_{300}$, $CFNb_{400}$, $CFNb_{500}$ and $CFNb_{600}$.

Figure 30 - SEM/EDS characterization of the sample CFNb. By: authors

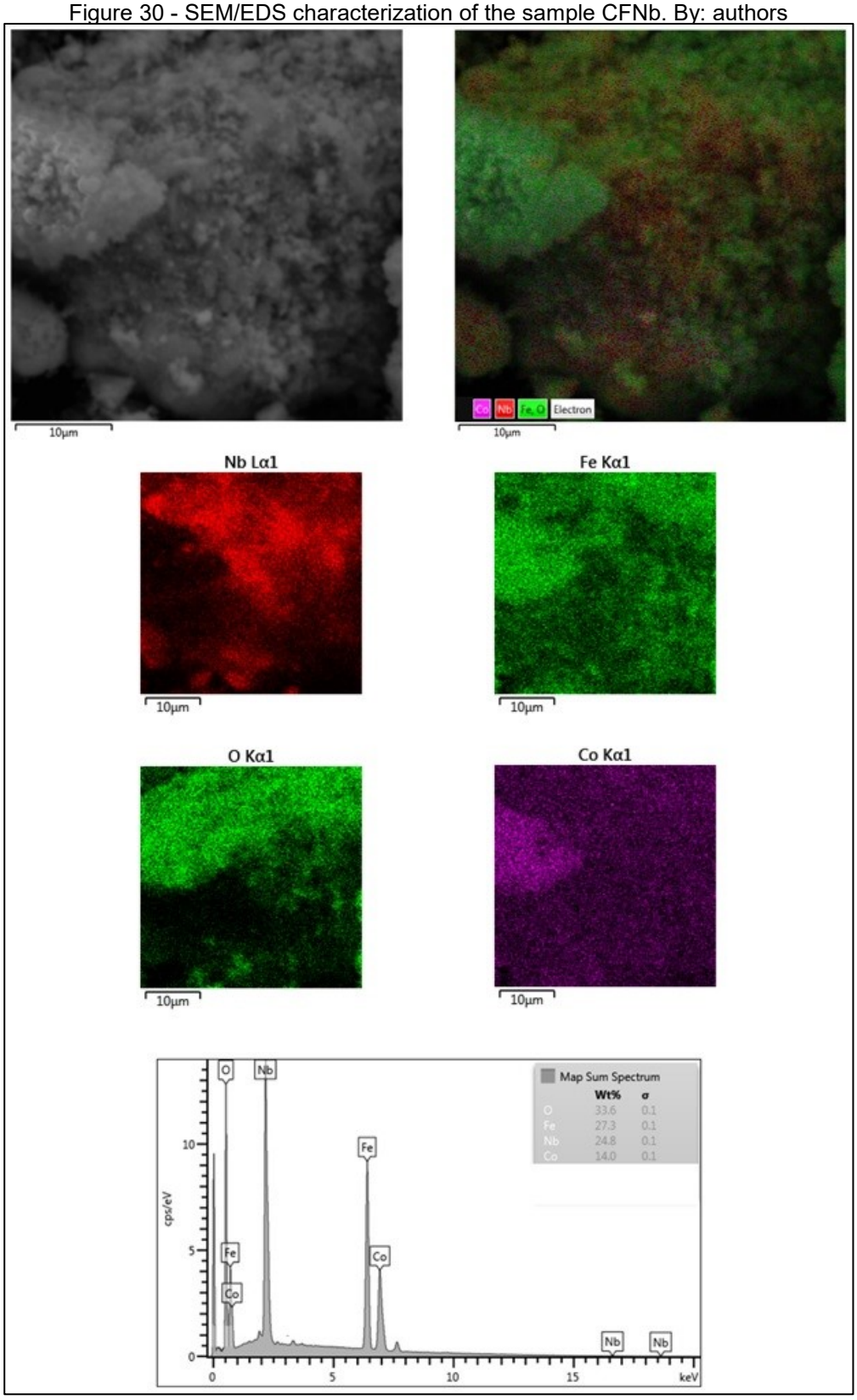

Figure 31 - SEM/EDS characterization of the sample $CFNb_{100}$. By: authors

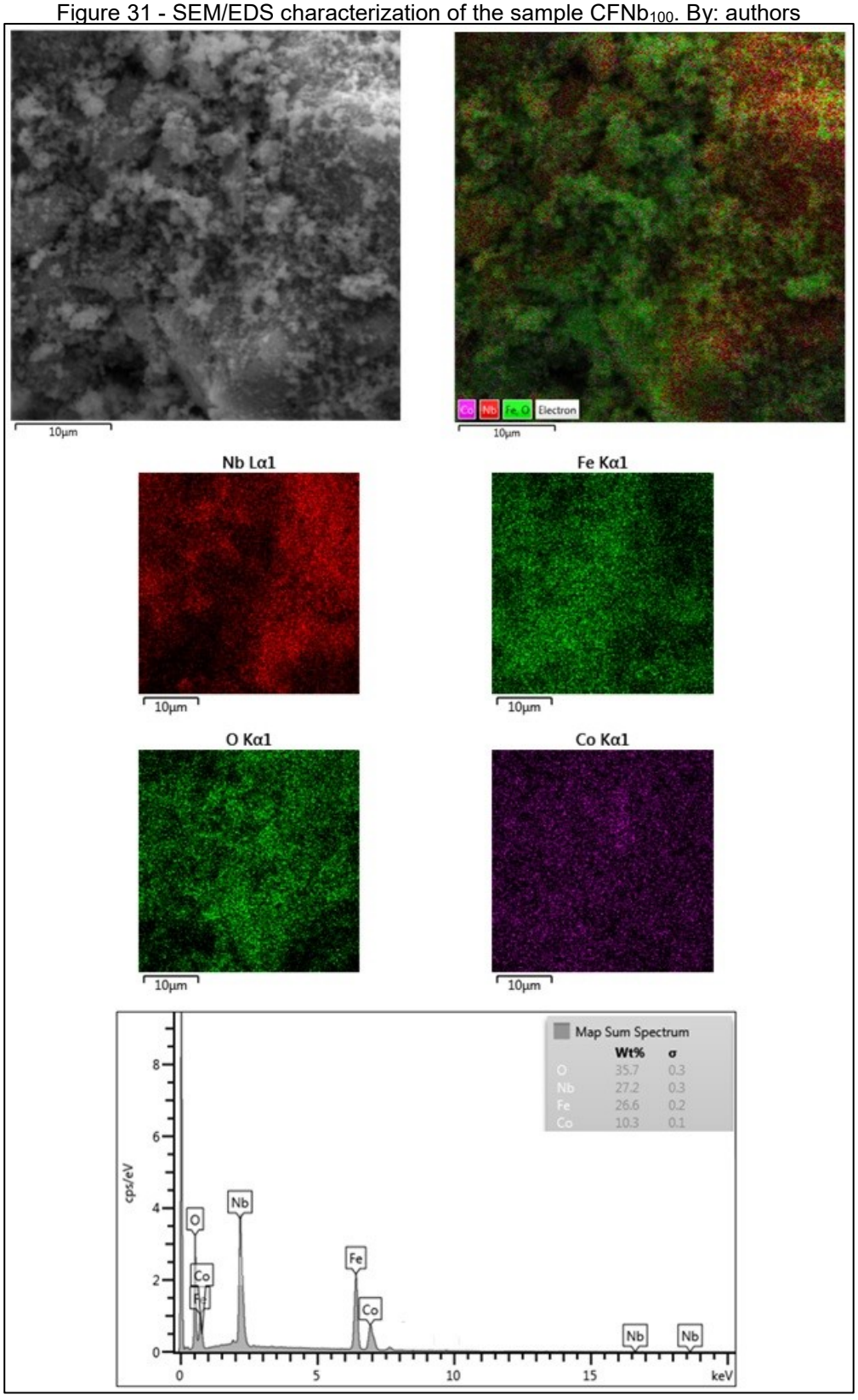

Figure 32 - SEM/EDS characterization of the sample $CFNb_{200}$. By: authors

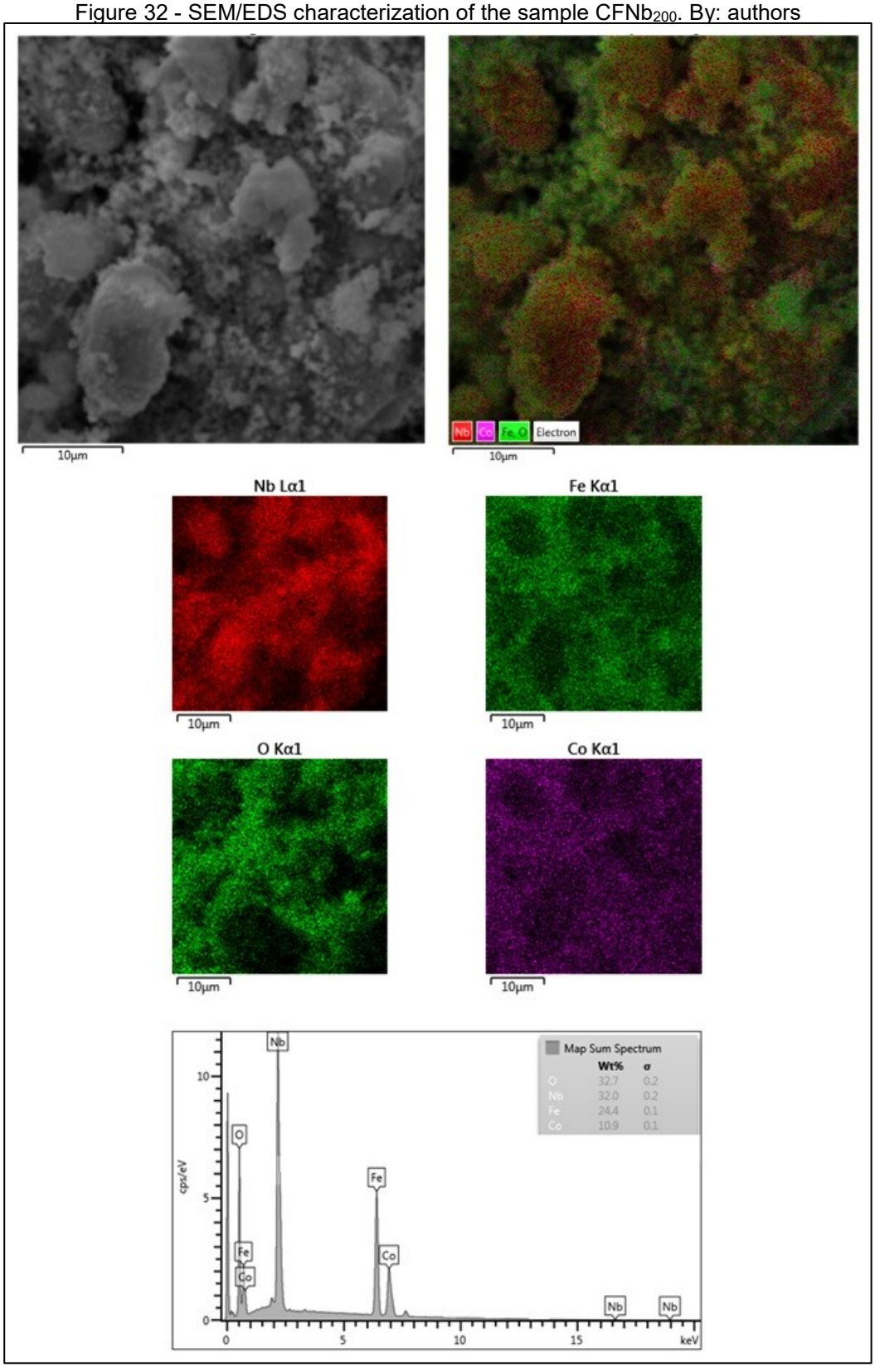

Figure 33 - SEM/EDS characterization of the sample $CFNb_{300}$. By: authors.

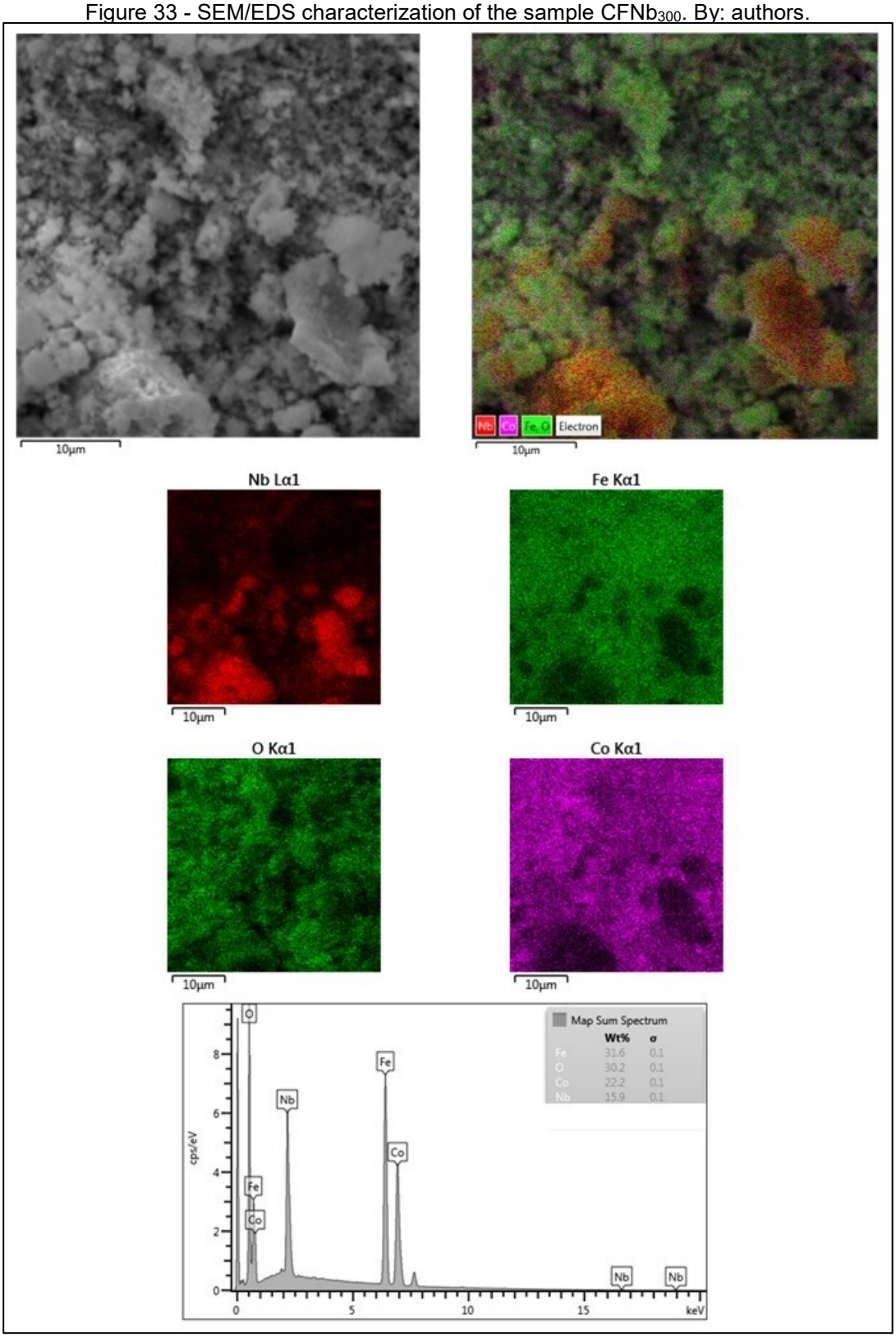

Figure 34 - SEM/EDS characterization of the sample $CFNb_{400}$. By: authors

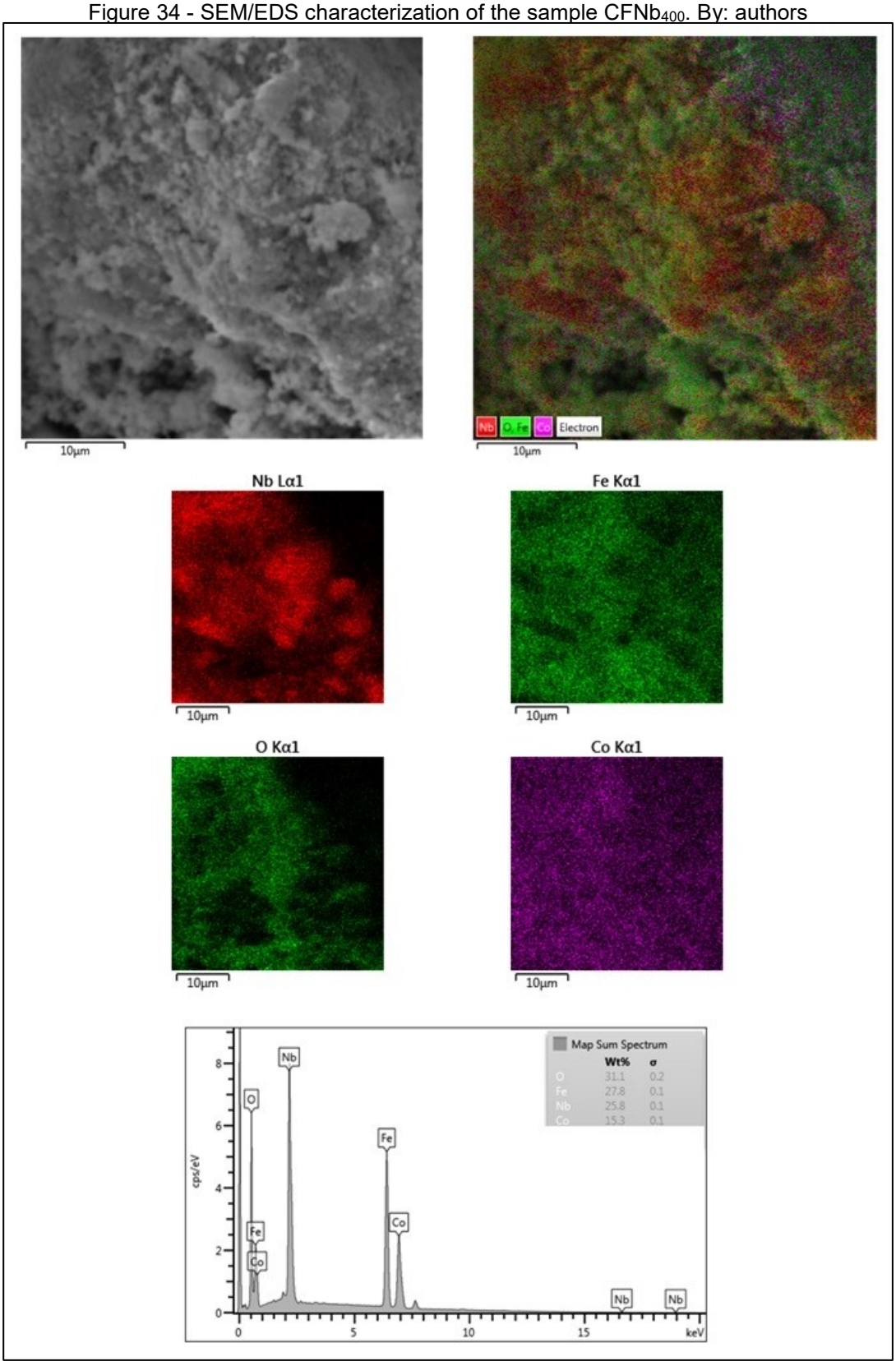

Figure 35 - SEM/EDS characterization of the sample $CFNb_{500}$. By: authors

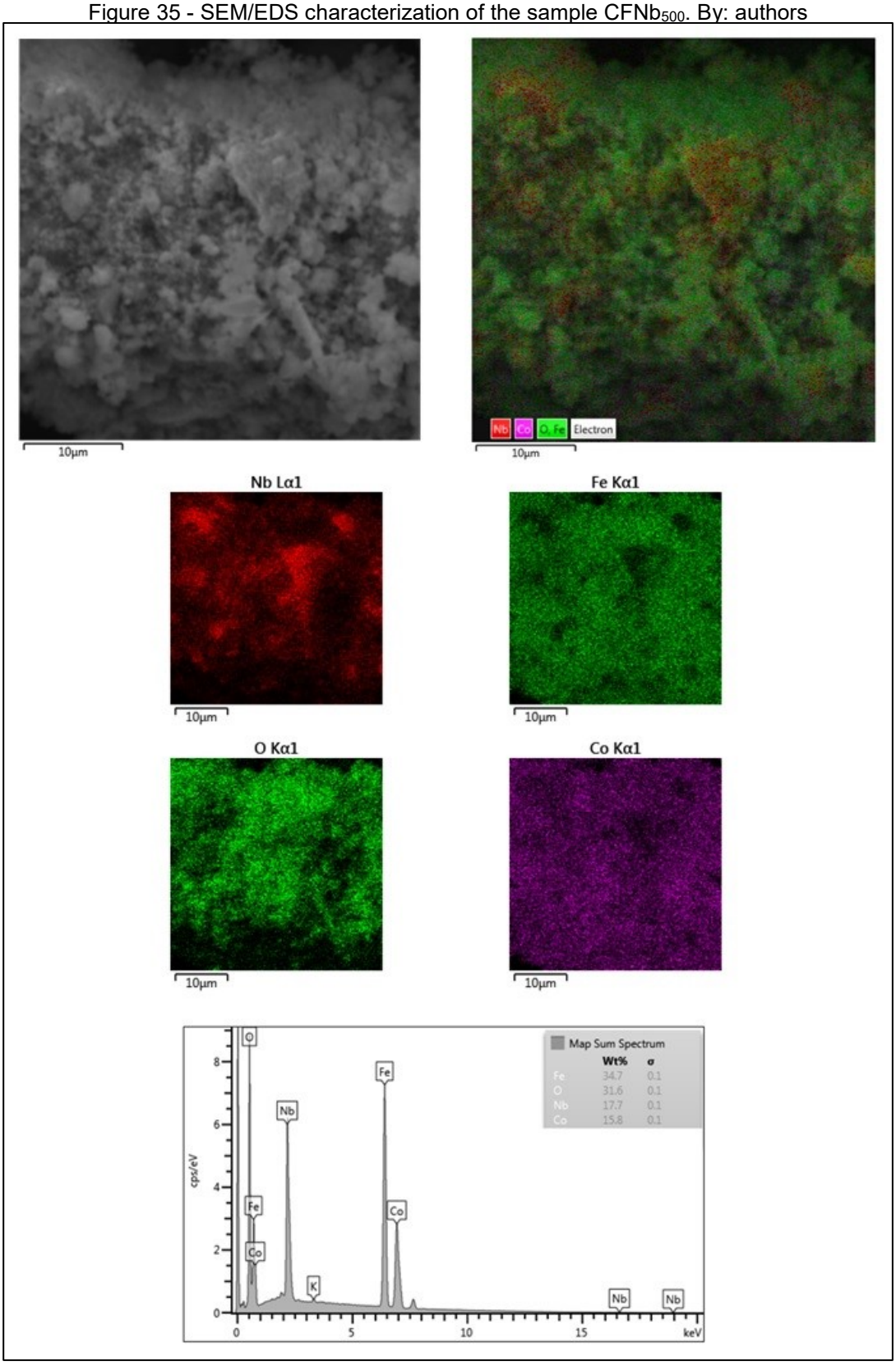

Figure 36 - SEM/EDS characterization of the sample $CFNb_{600}$. By: authors